



**HAL**  
open science

## Modeling of chloride spatial variability in a reinforced concrete wharf from on-site measurements

Romain Clerc, Franck Schoefs, Mestapha Oumouni, Othmen Ines, Stéphanie Bonnet

► **To cite this version:**

Romain Clerc, Franck Schoefs, Mestapha Oumouni, Othmen Ines, Stéphanie Bonnet. Modeling of chloride spatial variability in a reinforced concrete wharf from on-site measurements. ASCE-ASME Journal of Risk and Uncertainty in Engineering Systems, Part A: Civil Engineering, inPress, 10.1061/AJRUA6/RUENG-1214 . hal-04494998v2

**HAL Id: hal-04494998**

**<https://nantes-universite.hal.science/hal-04494998v2>**

Submitted on 24 May 2024

**HAL** is a multi-disciplinary open access archive for the deposit and dissemination of scientific research documents, whether they are published or not. The documents may come from teaching and research institutions in France or abroad, or from public or private research centers.

L'archive ouverte pluridisciplinaire **HAL**, est destinée au dépôt et à la diffusion de documents scientifiques de niveau recherche, publiés ou non, émanant des établissements d'enseignement et de recherche français ou étrangers, des laboratoires publics ou privés.

1 **Modeling of chloride spatial variability in a reinforced concrete wharf from on-**  
2 **site measurements**

3 **Romain CLERC**<sup>1</sup>, **Franck SCHOEFS**<sup>1</sup>, **Mestapha OUMOUNI**<sup>1</sup>, **Inès**  
4 **OTHMEN**<sup>2</sup>, **Stéphanie BONNET**<sup>2</sup>

6 <sup>1</sup> *Nantes Université, École Centrale Nantes, CNRS, GeM, UMR 6183, F-44000 Nantes, France*

7 <sup>2</sup> *Nantes Université, École Centrale Nantes, CNRS, GeM, UMR 6183, F-44600 Saint-Nazaire,*  
8 *France*

9 \* Corresponding author email: [franck.schoefs@univ-nantes.fr](mailto:franck.schoefs@univ-nantes.fr)

10

11

12

13

15 Chloride ingress by diffusion is the major deterioration process of reinforced concrete (RC) structures exposed  
16 to the marine environment. These structures have significant lengths or surfaces exposed to the outside  
17 environment. Due to the material variability (different concrete batches, vibrations) and exposure variability,  
18 the material experiences a spatial variability of the deterioration process. This paper presents the geostatistical  
19 analysis of in-situ chloride profiles, leading to the assessment of the spatial variability (SV) of both the chloride  
20 ingress itself and the parameters of the widely used Fick diffusion law (the average surface chloride content,  
21  $C_{sa}$ , and the average chloride diffusion coefficient,  $D_a$ ). 37 chloride profiles measured on both sides of the  
22 same spandrel beam of an RC wharf are studied, as well as the associated estimates of  $C_{sa}$  and  $D_a$ . From an  
23 initial selection of random field models, the geostatistical analysis consists in the evaluation of model  
24 parameters using a procedure that tests both data and model assumptions on the fly (ergodicity, stationarity,  
25 random field modeling). Combined with the calculation of information criteria for each model, this procedure  
26 allows to provide relevant geostatistical models for chloride ingress,  $C_{sa}$  and  $D_a$ , which render SV as well as  
27 measurement error. It is noteworthy that the estimation error can be neglected when focusing on the SV for  
28 the range of chloride content studied in this paper. The SV of the chloride content seems to depend on the  
29 depth, with a large variability within the convection zone, and much less and more stable in the diffusion zone  
30 with a practical range of about 70 cm. This order of magnitude is consistent with the range of SV calculated  
31 for  $C_{sa}$  (50 to 73 cm).

32 **Keywords:** Chloride ingress, Reinforced concrete, Marine environment, Spatial variability,  
33 Random field, Statistical analysis.

## 34 1. Introduction

35 Chloride ingress is among the main causes of degradation of reinforced concrete (RC) structures  
36 where the deterioration is more perceptible in marine environment. That leads to major maintenance  
37 costs (Bastidas-Arteaga & Schoefs, 2015; Stewart & Val, 2003). These structures offer to the  
38 environment important lengths or surfaces. Due to the variabilities of both the material (different  
39 concrete batches, vibrations) and exposure, they experience a spatial variability of their deterioration  
40 process. Accounting for realistic spatial correlation of the different parameters in structural safety  
41 models may lead to more realistic estimates on structural reliability and maintenance planning,  
42 knowing that reliability assessment is affected by spatial correlation (Schoefs et al., 2022; Stewart,  
43 2004; Stewart & Mullard, 2007). Moreover, quantifying this property allows optimizing inspection

44 meshing on a structure (Gomez-Cardenas et al., 2015; Oumouni & Schoefs, 2021b; Schoefs et al.,  
45 2017a).

46 The variability of the degradation parameters and their measurements can be described at  
47 different scales:

- 48 • the point scale, characterizing the repeatability of measurements;
- 49 • the local scale of the material, characterizing the heterogeneity of the material for a scale  
50 lower than the Representative Elementary Volumes (REV) associated with each of the  
51 quantities of interest (Hill, 1963);
- 52 • higher scales (structural elements, structure), characterizing the degree of spatial  
53 heterogeneity of the material and/or environmental conditions (exposure, loading, ...) for  
54 scales above the REVs.

55 The restitution of point and local variabilities requires a statistical modeling, translating the  
56 hypothesis of independence, respectively on (i) the measurements of parameters between distinct  
57 measurements and for a same measurement point and (ii) the parameter values between similar  
58 structures for the same REV dimension. The spatial variability (taking into account local and larger  
59 scales) cannot be solely captured by a statistical modelling because of the hypothesis of the existence  
60 of a certain degree of heterogeneity, i.e. spatial correlation, between measurements or between  
61 parameter values associated with different measurement points or REV on the same structure. This  
62 can only be translated by geostatistical modeling. The major challenge of those models is to determine  
63 stochastic properties of the Random Fields (RF), namely their marginal distributions, stationarity and  
64 the spatial correlations.

65 Chloride ingress has been investigated deeply since the 70's and it has been shown how  
66 complex is the process physically and chemically (Glasser et al., 2008; Kaushik & Islam, 1995; Ragab  
67 et al., 2016; Safhi et al., 2019; Wegian, 2010) and the role the material complexity (porosity) is

68 playing (Qu et al., 2021). For the moment, available models of transfer and knowledge don't allow  
69 to represent accurately the spatial variability of pollutant in concrete (Ravahatra et al., 2017). That is  
70 the main reason why direct or indirect assessment of chlorides in situ is the only way to measure,  
71 analyze and model the spatial variability of chloride ingress. Then, two kinds of quantities of interest  
72 can be considered:

- 73 • the total chloride content  $C$  at several depths;
- 74 • their mean diffusion parameters  $C_{sa}$  and  $D_a$ , estimated from profiles of chloride content.

75 During the last decades sensors have experiences significant progresses (Biondi et al., 2021;  
76 Torres-Luque et al., 2014, 2017; Watanabe et al., 2021; Zaki et al., 2015) but there are few concepts  
77 that measure the spatial distribution of chloride ingress (Fares et al., 2018; Lecieux et al., 2015, 2019)  
78 and their implementation is rare (Priou et al., 2019) even if their interest in terms of the value of  
79 information they provide was shown (Schoefs et al., 2022) especially because they allow to filter the  
80 signal (Oumouni & Schoefs, 2021a). Moreover, these sensors have to be installed at the building  
81 stage and are not suitable for existing structures.

82 That is the main reason why spatial variability is assessed through Non-Destructive Testing  
83 (NDT) tools or Semi-Destructive Techniques (SDT). On-site indirect assessment of chlorides through  
84 NDT-techniques is affected by errors of assessment and sensitivity to other parameters (humidity,  
85 temperature) which makes it difficult to assess the spatial variability of chlorides (Bonnet et al., 2017;  
86 Bourreau et al., 2019; Schoefs et al., 2023). This error affects the optimization of measurements for  
87 assessing spatial variability (Oumouni & Schoefs, 2021b). That is why, the rare studies are based on  
88 the semi destructive techniques (SDT) i.e. direct weighting of chlorides from cores (O'Connor &  
89 Kenshel, 2013; Othmen et al., 2018) reviewed 10 published studies from 2004 to 2016 with only 3  
90 concerning more than 30 measurements and in all cases the distance between measurement was too  
91 large in view to assess the spatial correlation. Two main quantities of interest are investigated:  
92 chloride content at a given depth and parameters of a model of chloride ingress after post-processing

93 of chloride profiles.

94       Because of the complexity and cost for making a large amount of cores in a beam, only a few  
95 amounts of data is available for each and the distance between cores is too large: 5 cores with a  
96 distance of about 1 m in the study of (O'Connor & Kenshel, 2013). That leads to a significant  
97 numerical error of assessment of the spatial correlation (Schoefs et al., 2017b). Moreover, the  
98 underlying assumptions for RF modelling that are stationarity and ergodicity are not checked. Finally,  
99 the error of measurement is usually not considered when identifying correlations. That is a drawback  
100 because it is well known that SDT measurements for existing structures (Schoefs et al., 2023) and  
101 even for concrete in laboratory (Bonnet et al., 2017; Hunkeler et al., 2000) are affected by a significant  
102 error. To overcome these limits, this paper relies on two pillars: first, a unique database and second,  
103 a geostatistical analysis that allows to provide geostatistical parameters (namely spatial correlation  
104 assessments as well as measurement error) by using a recent method of RF identification (SCAP1D,  
105 Clerc et al. 2019), that accounts for uncertainty of measurements, checks ergodicity and accounts for  
106 the non-stationarity of the RF.

107       Concerning the first pillar, marine structures can be exposed in various environments:  
108 atmospheric, spatter or splash, tidal and underwater (BS 6349-1:2000, 2000) which were defined  
109 according to the tide range (Bourreau et al., 2020). In this work, 30 cores carried out every 30 cm on  
110 the same 28-year beam (Othmen et al., 2018) are analyzed. The beam is located in the worst  
111 environment that is splash zone (Angst et al., 2009), and the cores are through its width giving access  
112 to profiles from each side i.e., exposure conditions (exposed, sheltered).

113       Concerning the second pillar, two objectives are targeted: the assessment of spatial variability  
114 of the total chloride content  $C$ , depending on depth and exposure on one hand and the assessment of  
115 the spatial variability of the mean diffusion parameters  $C_{sa}$  and  $D_a$  on the second one. First, taking  
116 benefit of the availability of  $C$  at several depth, the objective is to provide estimates of its geostatistical  
117 parameters and to answer the following questions: (i) Is the spatial variability (SV) of  $C$  a function of

118 depth? (ii) Is the SV of  $C$  a function of the exposure conditions? Second, knowing the age of the  
119 structure (28-year), geostatistical parameters of mean diffusion parameters are estimated to answer  
120 the following question: Is the SV of  $C_{sa}$  and  $D_a$  a function of the exposure conditions? The latter  
121 question arises because  $C_{sa}$  and  $D_a$  are directly dependent on the chloride profiles, which vary  
122 markedly between the exposed and sheltered faces.

123 Section 2 introduces the geostatistical formalism in a theoretical way before presenting a state  
124 of the art of RF modeling, simulation methods and spatial variability estimation methods. An attention  
125 is paid to the underlying assumptions of the estimation methods and to the consequences of their  
126 neglect on the estimated spatial variability, especially in the frequent case of non-stationary  
127 measurements due to spatially variable exposure conditions. Section 3 presents the structure and the  
128 available data. Sections 4 and 5 give the results at two levels: total chloride contents, and mean  
129 diffusion parameters of total chlorides. Section 6 concludes the paper with some extension to other  
130 structures or other exposures.

## 131 2. Geostatistical methods for spatial variability assessment of concrete structures

### 132 2.1. Modelling of spatial variability

#### 133 2.1.1. Random Field modeling

134 Practical modeling of spatial variability implies modeling spatially variable quantities of interest (QI)  
135 as Second-Order Intrinsic Stationary Random Fields (RF) (Chilès & Delfiner, 2012). Following the  
136 geostatistical formalism, such an RF  $Z$  is defined on a domain  $D^n$  of  $\mathbb{R}^n$  and on a probability space  
137  $(\Omega, A, P)$  such that:

- 138 •  $\forall \mathbf{x} \in D^n$ ,  $Z(\mathbf{x}, \cdot) = Z_{\mathbf{x}}$  is a multivariate random variable of  $\omega \in \Omega$  with a joint probability density  
139 function (PDF)  $f_Z(\mathbf{m}, \Sigma)$ , where  $\mathbf{m}$  and  $\Sigma$  are the mean vector and the covariance matrix of  $Z_{\mathbf{x}}$ ,  
140 respectively;

- 141 •  $\forall \mathbf{x} \in D^n$  and  $\forall \omega \in \Omega$ ,  $Z(\mathbf{x}, \omega) = Z_x^\omega$  is a realization of  $Z$  georeferenced by the vector  $\mathbf{x}$ , also  
 142 called a trajectory (in practice, a set of measurements from a unique structure and at a unique  
 143 time).
- 144 •  $\forall (h, \mathbf{x}) \in D^2$ ,  $\mathbb{E}[Z_{\mathbf{x}+h} - Z_{\mathbf{x}}] = 0$  and  $Var(Z_{\mathbf{x}+h} - Z_{\mathbf{x}}) = 2\gamma(h)$  where  $\gamma(\cdot)$  is the semi-  
 145 variogram function of  $Z$  and  $h$  is any distance-lag (distance between two points of  $D$ ).

146 This definition reflects both the variability of the input parameter between structures and its spatial  
 147 variability within the same structure, which are embedded in the covariance matrix  $\Sigma$  and the semi-  
 148 variogram.

149 In this paper, data are modeled as (i) unidimensional (ii) noisy (iii) trend-stationary (iv) Gaussian  
 150 Random Field (GRF). Indeed, (i) the data are unidimensional along the sides of the beam; (ii) if the  
 151 spacing between measurements is greater than the REV, the RF model must be able to reproduce the  
 152 point and local variabilities, which have no correlation structure and can be modeled by white noise;  
 153 (iii) materials and environmental conditions may vary along the sides of the beam. It is then very  
 154 likely that the mean of the quantities of interest will vary with space; (iv) GRFs are very convenient  
 155 because they allow modeling most natural variabilities (following normal or lognormal marginal  
 156 laws) with only a model for the mean and the covariance (Chilès & Delfiner, 2012).

157 Mathematically,  $\forall \mathbf{x} \in D^n$  we thus consider  $Z$  such that

$$Z_x = \mathbf{m}_x + W_x + Y_x \quad (1)$$

158 with  $\mathbf{m}_x$  a deterministic trend,  $W_x \sim N(\mathbf{0}, t \times \mathbf{1}_n)$  a white noise of variance  $t$ ;  $Y_x \sim N(\mathbf{0}, \Sigma_Y)$  a  
 159 centered GRF, i.e  $Y_x$  a multivariate normal variable such that

$$\forall (h, \mathbf{x}) \in D^2, \Sigma_{Y_{\mathbf{x}+h}, Y_{\mathbf{x}}} \equiv Cov(Y_{\mathbf{x}+h}, Y_{\mathbf{x}}) \equiv C_Y(h) \equiv s \times \rho_Y(h) \quad (2)$$

160 where  $C_Y(\cdot)$  is the covariance function of  $Y$ ,  $s$  is its variance,  $\rho_Y(\cdot)$  is its autocorrelation function, and  
 161  $h$  is any distance-lag between the data (equivalences due to the Second-Order Stationarity of the  
 162 GRFs).

163 This formalism is illustrated in Figure 1 and Figure 2, where trajectories, correlation plots,  
164 autocorrelation functions, and semivariograms are plotted for  $Y$  and  $Z$  respectively, defined such that:

165 1)  $Y_x \sim N(\mathbf{0}, \Sigma_Y)$  with  $\Sigma_{Y_{x+h,x}} = s \times \exp(-1.73\|h\|^2/r_{95})$ ,  $\rho_Y(h) = \frac{\Sigma_{Y_{x+h,x}}}{s}$ ,  $\gamma_Y(h) = s -$

166  $\Sigma_{Y_{x+h,x}}$ ,  $s = 10$  and  $r_{95} = 20$ ;

167 2)  $Z = W + Y$  with  $W_x \sim N(\mathbf{0}, t \times \mathbf{1}_n)$ ,  $\Sigma_{Z_{x+h,x}} = t \times \delta_{x+h,x} + \Sigma_{Y_{x+h,x}}$ ,  $\rho_Z(h) = \frac{\Sigma_{Z_{x+h,x}}}{s+t}$ ,

168  $\gamma_Z(h) = s + t - \Sigma_{Z_{x+h,x}}$ , and  $t = 5$  ( $\delta_{ij}$  is the Kronecker delta).

169 2.1.2. *Autocorrelation models and parameters*

170

171

### 172 3. Embedded Tables

173 Table 5 and Figure 1 present and illustrate the exponential and Gaussian autocorrelation functions,  
174 widely used in the literature. According to Equation (2), such functions are positive definite, so that  
175 they asymptotically decay as a function of the distance-lag  $h$ . The evolution of this decay is mainly  
176 determined by the value of their scale parameter  $a > 0$ , which parametrizes the extent of the spatial  
177 correlation, i.e. the distance threshold below which the QI are strongly correlated.

178 The distance at which events are weakly correlated is referred to as the inspection distance threshold  
179 with a spatial correlation threshold definition of 30% in (Schoefs et al., 2016). Several notations and  
180 parameters coexist in the literature to describe this threshold, sometimes with some confusion. In the  
181 case of isotropic fields, the following three notations are commonly used: (i) Cressie (1993, p. 118)  
182 proposed the fluctuation range  $\theta$ , which is defined as  $\theta = \int_{-\infty}^{+\infty} \rho(h)dh$ ; (ii) (Cressie, 1993, p. 88)  
183 proposed the practical range  $r_{95}$ , which is defined as  $\rho(r_{95}) = 5\%$  (see Figure 1 and Figure 2); (iii)  
184 many authors proposed the correlation length  $l_c$ , which is not strictly defined and alternatively taken  
185 to be equal to  $a$ ,  $\theta$ ,  $r_{95}$  or some other particular range. In order to avoid any confusion and to facilitate  
186 comparison and interpretation, we give in

187

## 188 4. Embedded Tables

189 Table 5 the expression of  $\theta$  and  $r_{95}$  as a function of  $\alpha$  for the exponential and Gaussian models and  
190 the **corresponding** autocorrelation values  $\rho$ . Note that **in** Figure 1  $Y$  is obtained from a Gaussian  
191 autocorrelation function.

### 192 4.1. Identification of spatial variability from measurements

#### 193 4.1.1. Empirical identification

194 RF models behind a trajectory can be identified in **the** case of its *ergodicity*, which can be seen as a  
195 mixture of stationarity and asymptotic independence. In **this** case, **the spatial** variability can be  
196 assessed from empirical representations of the **semivariogram**, the covariance function, or the  
197 autocorrelation function, called **the** empirical **semivariogram**, covariogram and autocorrelogram,  
198 respectively.

199 The **Semivariogram**, denoted  $\hat{\gamma}(h)$ , is used **because** its **estimation** does not require **complementary**  
200 ones (**such as** mean or variance), and it allows to visually identify (i) **the** Second-Order Stationarity  
201 property, (ii) **the** ergodicity property, and (iii) **the** presence and magnitude of local variabilities.  
202 Indeed, (i)  $\hat{\gamma}(h)$  asymptotically tends **to the** variance for Second-Order Stationary RF, **while otherwise**  
203 whereas it increases with  $h$ ; (ii) **ergodicity** is verified **when**  $\hat{\gamma}(h)$  reaches an asymptote in the limit of  
204 half of the domain  $D$  (Cressie, 1993, p. 57); (iii) white noise is easily identified by a *nugget effect*,  
205 i.e. a non-zero value for  $h = 0$  (see Figure 2).

206 **A common** estimator of  $\hat{\gamma}(h)$  is defined by Equation (3) for a given trajectory  $Z_x^\omega$ , where  $S_h$  is the set  
207 of pairs  $(x_p, x_q)$  of  $D^2$  that are **away** from  $h$  modulo a given tolerance, and  $N_h$  is the cardinal of  $S_h$ .

$$\hat{\gamma}(h) = \frac{1}{2N_h} \sum_{(x_p, x_q) \in S_h} (Z_{x_p}^\omega - Z_{x_q}^\omega)^2 \quad (3)$$

208 We point out that when  $h$  becomes close to the dimension of  $D$ , statistical inference is no longer  
209 valid because the number of point pairs **away** from  $h$  is very small. Therefore, geostatisticians  
210 recommend plotting this graph only for **distances**  $h$  such that  $N_h \geq 30$  (Cressie, 1993). In practice,

211 in civil engineering, several authors recommend limiting to values of  $h$  less than half of the size of  
212 the domain (Arnaud & Emery, 2000, Schoefs et al., 2016).

#### 213 4.1.2. Estimates of model parameters

214 Once an RF model is selected from empirical identification, its parameters (collected in a vector  $\mathbf{p}$ )  
215 must be estimated. Several methods are available:

- 216 • Maximum Likelihood Estimation (MLE), which allows to estimate  $\mathbf{p}$  from raw data, given an RF  
217 marginal distribution model, and as the following properties: (i) asymptotically unbiased, (ii)  
218 consistent, (iii) equivariant, (iv) asymptotically efficient, and (v) asymptotically normal  
219 (Wasserman, 2004, para. 9.4);
- 220 • Least-Squares Estimate (LSE), which allows estimating  $\mathbf{p}$  from semivariogram, covariogram or  
221 autocorrelogram given models of them;
- 222 • Weighted LSE (WLSE), similar to LSE, where each of the residuals is weighted by its variance.  
223 This allows to increase the weight of the residuals computed from many data (low distance-lag  $h$   
224 values, for which  $N_h$  is larger).

225 Usually, LSE and WLSE fit the covariograms well and the use of WLSE implies a better description  
226 of them for small distances, associated with more data<sup>1</sup>. However, covariograms are not necessarily  
227 representative of the effective covariance parameters of the field, which can lead to significant relative  
228 errors in their estimation. Because it considers only raw data, MLE provides more accurate estimates,  
229 with smaller relative errors. The trade-off is computational time, as MLE is more time consuming  
230 than WLSE and LSE, up to 10 times faster. Therefore, and because it is *a priori* complex to have an  
231 initial idea of the scale parameter, a two-phase estimation method of Second-Order Stationary RF  
232 parameters is preferred:

---

<sup>1</sup> In this case,  $\gamma(h) = 1 - C(h)$ , so estimates on the covariogram or the semivariogram are equivalent.

- 233 1. **WLSE** pre-estimation of the parameters with the following initial values: (i) for  $s$ , the empirical  
 234 variance; (ii) for  $a$ , a value such that the fluctuation scale is less than a quarter of the maximum  
 235 lag-distance (so as to respect the ergodic assumption);
- 236 2. MLE estimation of the parameters **using the Nelder-Mead simplex minimization algorithm with**  
 237 **the WLSE estimates as initial values.**

238 This approach allows to obtain accurate estimates while minimizing the cost of the MLE due to the  
 239 definition of initial values close to the real values of the parameters (Clerc et al., 2019, para. 4.4).

#### 240 4.1.3. Choice of best RF model

241 Although **the plot of the** empirical semi-variogram allows **the selection of an** RF model, its estimator  
 242 nature **leads to** an imperfect representation of the SV. This is all the **more true** when the number of  
 243 measurements is small. **Therefore**, when there is insufficient scientific evidence to support a specific  
 244 RF model for a **QI**, which is the case for chloride content and diffusion parameters (Gomez-Cardenas  
 245 et al., 2015), we can rely on data-based methods **for model selection.**

246 In the following, the Akaike **I**nformation **C**riterion (AIC) is preferred **because** it is much more robust  
 247 than the  $R^2$  coefficient of determination (Burnham & Anderson, 2010). The AIC allows to compare,  
 248 with the parsimony criterion, the relevance of any RF model  $M_Z$  with  $K$  parameters  $p_{1,\dots,K}$  to describe  
 249 the hidden RF  $Z$  at the origin of a set of  $n$  data  $Z_x^\omega$  (**e.g.**, a trajectory). This criterion assumes that the  
 250 best model is the one that **provides** the most accurate description with the fewest possible parameters  
 251 (Burnham & Anderson, 2010, para. 1.4).

252 **In particular, when**  $n/K < 40$  and (which is the case **below**) we use the corrected information  
 253 criterion (**AICC**). When the  $\mathbf{p}$  estimate  $\hat{\mathbf{p}}$  is computed with MLE, it writes:

$$254 \quad AIC_c = \underbrace{-2 \ln(L(\hat{\mathbf{p}}|Z_x^\omega)) + 2K}_{AIC} + \underbrace{\frac{2K(K+1)}{n-K-1}}_{\text{correction}}$$

255 **where**  $L(\hat{\mathbf{p}}|Z_x^\omega)$  **is** the likelihood of  $\hat{\mathbf{p}}$  with respect to the data. The best model among a set of  
 256 considered models is then the one that minimizes the **AICC**, **i.e.** the one that has both a high goodness  
 257 of fit (high likelihood) and a limited complexity (limited number of parameters).

258 In practice, the easiest way to compare the relevance of models based on their AICC is via the  
259 Evidence Ratio (ER) (Burnham & Anderson, 2010, para. 2.10). This is defined such that, for any  
260 model  $M_{Z,i}$  among  $N_m$  models,

$$ER_i = \exp\left(\frac{1}{2}\left[AICC_i - \underbrace{\min_{j=1,\dots,N_m}(AICC_j)}_{\text{best a priori model}}\right]\right)$$

262 The ER is therefore 1 for the best *a priori* model and grows exponentially as the models become less  
263 fit. From an expert perspective, an ER of 2 for a given model does not justify preferring the best a  
264 priori model over it, whereas an ER of 18 clearly favors the best a priori model (Burnham &  
265 Anderson, 2010, para. 2.10).

#### 266 4.1.4. SCAP1D: a robust estimation procedure

267 The methods presented assume an adequate RF model to avoid estimation errors: without modeling  
268 precautions, they are only valid under the condition that the data can be described by an SSO and  
269 ergodic RF. However, since classical regression techniques coupled with generic autocorrelation  
270 models can easily approximate autocorrelograms and covariograms, the estimation of RF model  
271 parameters is typically performed by LSE on raw data without prior verification of these two  
272 hypotheses (O'Connor & Kenshel, 2013; Ravahatra et al., 2017; Schoefs et al., 2016). Such a  
273 procedure can then lead to significant errors, in especially in the estimation of the scale parameter  $a$ ,  
274 and especially in cases of non-stationarity in the mean and/or significant measurement noise. This  
275 point is demonstrated in a case study by (Clerc, 2021, p. 143): from a given realization of a standard  
276 GRF, adding a noise and/or a mean trend and performing an LSE of  $a$  without prior verification of  
277 the SSO and ergodic hypotheses led to estimation errors of up to 994%.

278 To avoid these errors, we use here the SCAP-1D procedure<sup>2</sup> (Clerc et al., 2019). Based on previously  
279 presented tools, it allows to estimate, from a single trajectory with few measurement points, the

---

<sup>2</sup> Spatial Correlation Assessment Procedure for Unidimensional Data

280 parameters of a unidimensional noisy trend-stationary RF with piecewise polynomial mean, constant  
281 variance and constant autocorrelation model.

282 The concept of SCAP-1D is to ensure the reliability of the parameters' estimates by testing and  
283 validating the following hypotheses:

- 284 • *H1*: validity of the RF mean model and its parameter estimates, i.e. Second-Order Stationarity of  
285 the centered RF;
- 286 • *H2*: validity of both the joint PDF and autocorrelation function models of the RF and of the  
287 estimation of their parameters; i.e., normality of the standard source GRF, obtained by  
288 isoprobabilistic transformation of the RF from estimates considering the *a priori* model;
- 289 • *H3*: ergodicity of the trajectory; i.e., non-correlation of the data at infinity or determination of all  
290 geostatistical parameters from this trajectory.

291 The SCAP-1D flowchart is shown in Figure 3. It is divided into four consecutive steps, which can be  
292 repeated if the estimates do not validate the hypotheses on the RF model:

- 293 • *Step I) Choice of SCAP-1D parameters*, namely piecewise polynomial mean model (regression  
294 degree, number of changepoints), RF joint PDF and autocorrelation function. We recommend to  
295 plot the trajectory, its histogram and its experimental semivariogram to facilitate this step.
- 296 • *Step II) Estimation of the mean and geostatistical parameters*: changepoints in the mean and their  
297 significance are determined using the PELT (Pruned Exact Linear Time) optimal partitioning  
298 algorithm of (Killick et al., 2012). Estimation of the RF parameters is then performed using the  
299 approach presented in 4.1.2<sup>3</sup>.
- 300 • *Step III) Checking of the underlying mathematical hypotheses*: the plausibility of the estimated  
301 model is verified by checking ergodicity and performing stationarity tests (DF-test (Dickey &  
302 Fuller, 1981), KPSS-test (Kwiatkowski et al., 1992)) and normality tests ( $\chi^2$ , KS-test  
303 (Kolmogorov-Smirnov)) on the standardized trajectory, based on the Step II estimates.

---

<sup>3</sup> or by WLSE on the experimental semivariogram in the case of non-explicit density models.

304 • *Step IV) Analysis*: based on the Step III tests, the model selected in Step I and the estimates made  
305 in Step II are either accepted (algorithm stops) or rejected (modification of Step I parameters is  
306 required).

307 In Step III, the standardization of the trajectory is done by the Cholesky transformation, taking into  
308 account either:

309 • the empirical covariance matrix: in this case, we only test H1, since the tests results depend only  
310 on the data and the estimates of the mean. The tests are then called  $\Sigma_{exp}$ -tests;

311 • or the modeled covariance matrix: in this case, we test H1 to H3 together, since the tests results  
312 depend on the total estimates. The tests are then called  $\Sigma_{mod}$ -tests.

#### 313 4.1.5. Interpretability criterion

314 In Step IV of SCAP-1D, the estimates must be analyzed for their physical consistency. In particular,  
315 an interpretability criterion can be defined for the estimated practical range. The point is to ensure,  
316 with respect to the distance  $\Delta x$  between measurements, that the variability thus described is indeed a  
317 spatial variability and not a local or point variability. This is illustrated in Figure 4, where the  
318 Gaussian autocorrelogram is plotted on a measurement grid of step  $\Delta x = 5$  for three practical range  
319 values ( $r_{95} < 2\Delta x$ ,  $r_{95} \simeq \Delta x$ , and  $r_{95} > 2\Delta x$ ):

320 • when  $r_{95} \geq 2\Delta x$  (curves c3 and c2): the variability described is spatial variability, since there is  
321 at least one significant intermediate spatial correlation value between the total correlation of a  
322 point with itself and the minimum 5% correlation associated with the practical range;

323 • when  $r_{95} < 2\Delta x$  (curve c1): the variability described may be local or point variability since there  
324 is no significant intermediate spatial correlation value to account for the spatial variability.

325 Therefore, care will also be taken to ensure that the criterion  $r_{95} \geq 2\Delta x$  is met when applying SCAP-  
326 1D<sup>4</sup>.

## 327 5. Presentation of the structure and the measurements

### 328 5.1. Presentation of the wharf, the beam and its material

329 The reinforced concrete beam inspected within the framework of the APOS research project is a T  
330 hyperstatic beam called "J-beam", whose dimensions and reinforcement are shown in Figure 5. It is  
331 located on lane 51 of the gangway 5 of the Montoir-de-Bretagne coal terminal (Loire-Atlantique  
332 department, France) with GPS coordinates: 47.32°N, -2.17°E. This terminal, built between 1981 and  
333 1983 on the banks of the Loire and less than 7 km from the Atlantic Ocean, is 234.4 m long and 20.7  
334 m wide and is located at +8.40 m NGF (Figure 6). This proximity to the ocean implies the existence  
335 of a tidal phenomenon with an amplitude of 5.80 m and a salinity of the water corresponding to  
336 maritime conditions at high tide (about 30 g Cl<sup>-</sup>/L). Thus, at the highest tidal coefficients, the lower  
337 face of beam J, located 5.80 m above the level of the Loire, is in contact with the water for about 2  
338 days per month. Finally, one of the peculiarities of the J-beam is its location at the edge of the quay.  
339 It has a side exposed to the wetting-drying cycles, marked Ext, and a sheltered side, marked Int (see  
340 Figure 6).

341  
342 Data from the construction archives indicate that the concrete used to build the structure is a Portland  
343 cement concrete CEMI 42.5N dosed at 350 kg/m<sup>3</sup>. The mass fraction of  $m_{cl}$  clinker is therefore  
344 higher than 90% and that of secondary constituents such as gypsum does not exceed 5%. The  
345 aggregates used are sand 0/6, and gravel 5/10 and 10/25. Concrete water porosity  $\varepsilon$ , measured on the  
346 central part of 5 specimens used for chloride titration, was 13.7% on average, with minimum and

---

<sup>4</sup> This criterion is constructed similarly to that of (Der Kiureghian & Ke, 1987) on the ability of a discretization grid to reproduce the spatial variability properties of an RF.

347 maximum values of 11.3% and 15.9%, respectively. The average compressive strength  $f_{cm}$ , measured  
348 on 4 specimens of 5 cm diameter and 10 cm length, was 43.5 MPa, with minimum and maximum  
349 values of 38.5 MPa and 48.9 MPa, respectively.

## 350 **5.2. Total chloride content measurements at 28 years**

### 351 *5.2.1. Available data set*

352 Chloride content measurements were performed on 30 through cylindrical cores extracted on the J-  
353 beam at the same height of 30 cm and with a lateral spacing of 30 cm (see Figure 7) (Othmen et al.,  
354 2018). The extraction was performed in 2011-2012, after 28 years of exposure. From initial  
355 dimensions of 50 mm in diameter and 400 mm in length, each core was divided into 5 slices  
356 (identified in Figure 7). Slices 1, 2, 4 and 5 were used to determine the chloride profiles according to  
357 the procedure recommended by the RILEM TC 178-TMC (Vennesland et al., 2013). Slices 1 and 2  
358 are related to the outer side (collected in Ext specimens) and slices 4 and 5 are related to the inner  
359 side (collected in Int specimens). While deep slices 2 and 4 were 40 mm thick with measurements in  
360 10 mm increments, slices 1 and 2 were 45 mm thick with measurements in 5 mm increments to  
361 capture the value at the surface. Slice 3 was used for further investigations such as porosity,  
362 compressive strength and estimation of the initial chloride content. Out of a total of 30 samples per  
363 side, 16 were usable on the Ext Face (53%), and 21 on the Int Face (70%). Furthermore, of the 555  
364 total chloride contents of the 30 samples considered, only 460 were usable (83%, or 51% of the total  
365 originally planned measurements).

366  
367 Figure 9 hereafter then represents the remaining set of total chloride measurements at 28 years finally  
368 considered (marked C in the following). The evolution of the empirical mean and standard deviation  
369 by depth and by face is shown in Figure 8.

### 370 5.2.2. Constitution of trajectories

371 In the following, the evolution of the SV of  $C$  is analyzed as a function of depth and exposure  
372 conditions. SCAP-1D is then applied to horizontal trajectories of measurements made on the same  
373 face and at the same embedding depth  $z$ . The estimation of geostatistical parameters for each  
374 trajectory then allows plotting their evolutions as functions of  $z$  and exposure face. This study  
375 principle is illustrated in Figure 9.

### 376 5.3. Average diffusion parameters at 28 years

377 The 37 total chloride profiles were post-processed to determine the associated Fick's second law  
378 average diffusion parameters at the reference time  $t_r$  of 28 years, denoted  $C_{sa}$  and  $D_a$ . The fitting  
379 procedure to the peak of the profiles is described in (Othmen et al., 2018) and implemented in  
380 (Schoefs et al., 2023). Thus, one trajectory for each diffusion parameter per side is constructed at a  
381 height of 30 cm. These include 16 points for the Ext Side and 21 points for the Int Side, with a  
382 minimum distance of 30 cm between measurement points.

383 Table 6 summarizes this information and Figure 10 shows the trajectories. Note that the log function  
384 is applied to each parameter to (i) simplify the representation and visual analysis as they are assumed  
385 to be lognormally distributed, (ii) use identification procedures (see section 4.2) available for  
386 normally distributed random fields.

## 387 6. Spatial variability estimates of total chloride content in J-beam and physical 388 understanding

### 389 6.1. Preamble: trajectories conditioning (kriging, debiasing)

390 Taking into account the non-usable or missing measurements per sample and in order to take into  
391 account the maximum number of points per trajectory, these are first enriched by ordinary kriging of  
392 the available data (Baillargeon, 2005, Chapter 4; Chilès & Delfiner, 2012, Chapter 3). The preliminary  
393 plot of the raw trajectories does not show any obvious non-stationarity (Figure 11), and the  
394 expectation of the associated RF is not known.

395 The kriging is then performed from the Weighted Least-Square Estimate (WLSE) identification on  
396 the semivariograms of the initial trajectories. We consider an exponential covariance model and the  
397 presence of an additive measurement error, identified by (Bonnet et al., 2017). In addition, (Bonnet  
398 et al., 2017) also identified a measurement bias  $b = 0.37 \times 10^{-3}$  (kg/kg concrete) associated with the  
399 measurement protocol used and with human errors during its implementation. All the measurements  
400 are therefore debiased before kriging so that the data considered are now  $C + b$ . In order to limit the  
401 influence of the kriged data on the estimation of the SV of  $C$ , only the trajectories for which their  
402 proportion is less than 25% are considered.

403 In total, 13 trajectories with 16 points can be considered on the Ext side ( $z \in [2.5; 75]$  mm) and 12  
404 trajectories with 21 points on the Int side ( $z \in [2.5; 65]$  mm). The number of kriged data per trajectory  
405 is detailed in Table 1 in the Appendix, and the selected debiased trajectories are shown in Figure 12.  
406 Less than 25% of the data are kriged to 65 mm depth for both sides. We point out that due to the  
407 absence of measurements on the abscissae of the non-exploitable specimens, the trajectory grids are  
408 irregular, with 30% of measurements missing for the Int side and 53% for the Ext side. The  
409 performance of the SCAP-1D normality tests is therefore affected (Clerc et al., 2019), and special  
410 care must be taken to ensure the consistency of the estimation results.

## 411 6.2. Geostatistical pre-study and choice of parameters (Step I):

412 We recall that the studied trajectories are debiased. We then denote  $\tilde{Z}$  the RF of  $C$  such that

$$413 \tilde{Z} = Z - b \quad | \quad b = -0.37 \times 10^{-3} \text{ kg/kg concrete} \quad (4)$$

414 In addition, (Othmen et al., 2018) have previously determined that the marginal law of  $C$  is lognormal,  
415 and (Bonnet et al., 2017) have identified the "measurement error" introduced by the measurement  
416 protocol, but only for a mortar. This is distributed according to a generalized extremum law  
417 (GeV, (Johnson et al., 1995, p. 3)) with the parameters  $k = 0.16$ ,  $\sigma = 9.3 \times 10^{-5}$ , and  $\mu =$   
418  $-8.4 \times 10^{-5}$ . (Schoefs et al., 2023) recently pointed out that the error model varies with chloride  
content. Consequently, the error should vary according to each trajectory. For simplicity, it is

419 considered constant in this paper and its standard deviation is an average of the potential standard  
420 deviations (Schoefs et al., 2023).

421 The best-fitting RF model for  $\tilde{Z}$  is then the sum of a log-normal RF  $Y$  and a GeV random variable  
422  $W$  such that, according to Equation (1),  $Z = Y + W$ .

423 However, the joint PDF of such an RF is not explicit, and SCAP-1D cannot simply be applied.

424 The small number of points per trajectory also precludes an estimation by WLSE on semivariograms  
425 (see 4.1.2).

426 Two modeling compromises are then possible in order to ensure explicitness:

- 427 • *Model a*: consider a normal marginal distribution of the total chloride content and a normal  
428 distribution of the error, so that

$$\tilde{Z} \sim \underbrace{N(\mu(x), s, R(a))}_{G^1} + t \cdot N(0, I) \quad (5)$$

429 where  $s$  and  $t$  are respectively the empirical variance of the signal and the error and  $R(a)$  is the  
430 autocorrelation matrix.

- 431 • *Model b*: do not consider the measurement error, whose standard deviation ( $1.55 \times 10^{-4}$  kg/kg  
432 concrete according to the model of (Bonnet et al., 2017) ) would induce a maximum CoV of 8.3%  
433 (on trajectory 13; Ext side,  $z = 75$  mm). For this model,

$$\tilde{Z} \sim \exp\left(\overbrace{N(\mu(x), s, R(a))}^{LN}\right)_{G^2} \quad (6)$$

434  $G^1$  and  $LN$  are then the RF describing the SV of  $C$ , with  $G^2$  being the source GRF of  $LN$ .

435 Since the first approximation of the maximum CoV according to the model of (Bonnet et al., 2017)  
436 is significant, we then apply SCAP-1D considering both models, so that :

- 437 • if the Signal-to-Noise Ratio (SNR) associated with model  $a$  is low, the error is not negligible and  
438 model  $a$  is retained;
- 439 • if the SNR associated with model  $a$  is high, the error is considered negligible and model  $b$  is  
440 retained.

441 Due to the absence of non-stationarities visible in Figure 12, the trajectories are *a priori* assumed to  
 442 be stationary, so that  $\mu(x) = \mu$ . We also recall that the model of the autocorrelation function chosen  
 443 for  $G^1$  and  $LN$  is exponential. According to (Chilès & Delfiner, 2012, p. 106), to guarantee such  
 444 a model for the autocorrelation function  $\rho_{LN}(a)$  of  $LN$ , the autocorrelation function  $\rho_{G^2}$  of  $G^2$  must  
 445 be written as follows

$$\rho_{G^2}(\cdot) = \ln(\rho_{LN}(\cdot) \cdot [e - 1] + 1) \quad (7)$$

446 According to (Chilès & Delfiner, 2012, p. 106), the mean  $m_{LN}$  and the variance  $\sigma_{LN}^2$  of  $LN$  are  
 447 then written as follows

$$m_{LN} = \exp\left(\mu + \frac{1}{2}s\right) \quad (8); \quad \sigma_{LN}^2 = m_{LN}^2(\exp(s) - 1) \quad (9)$$

### 448 **6.3. Model a: Parameter estimation, hypothesis testing and analysis (Steps II, III** 449 **and IV)**

450 Preliminary note: Prior to estimation, the trajectory data, of order  $10^{-3}$ , are multiplied by a factor  
 451  $k = 10^4$  to facilitate the convergence of the MLE. The estimates of  $t$ ,  $s$  and  $\mu$  are then transformed  
 452 accordingly before analysis.

453 Table 2 in the Appendix details the results of the SCAP-1D implementation considering model *a*.  
 454 Only the results of the  $\Sigma_{mod}$ -tests are considered due to the small number of points per trajectory.  
 455 Analyzing these, the estimates for trajectories 4 and 5 are rejected due to the rejection of the  
 456 stationarity hypothesis by the KPSS-test and because the estimated error and practical range are  
 457 zero and well below  $2\Delta_x$ , respectively, so that the spatial correlation of the data cannot be described  
 458 (see 4.1.5). This is also the case for trajectories 2, 11, 12, and 13 and can be explained by their very  
 459 small number of points. Similarly, the estimates associated with trajectories 15, 17, and 24 are not  
 460 considered because the estimated practical range is zero. Finally, no valid and convergent estimate  
 461 can be obtained for trajectory 14. As a first step, for each selected trajectory, we plot the estimates

462  $\hat{\mu}$  of the mean with their 95% MLE-based confidence intervals in Figure 13 (a)<sup>5</sup>, and the estimates  
463  $\sqrt{\hat{s} + \hat{t}}$  of the standard deviation, for which the distribution is unknown, in Figure 13 (b). We then  
464 note that these are consistent with the statistical mean and standard deviation profiles previously  
465 plotted in Figure 8: the values estimated by kriging (see 4.1) do not produce perturbations of these  
466 statistical estimates.

467 As a second step, we plot in Figure 14 (a) the standard deviation estimates  $\hat{t} = \sqrt{\hat{t}}$  and  $\hat{\sigma} = \sqrt{\hat{s}}$  of  
468 the error and signal, respectively, and the standard deviation  $\tau_\varepsilon$  associated with the error model of  
469 (Bonnet et al., 2017). Trajectories for which the estimated error is zero are not considered. We then  
470 compare the roots of the experimental SNRs  $\hat{t}/\hat{s}$  and the fixed error SNRs  $\tau_\varepsilon^2/\hat{s}$  in Figure 14 (b).  
471 Thus, we find that 75% of the roots of the experimental SNRs are greater than 100 and show no  
472 specific trend along. The fixed error SNRs are logically lower than the experimental ones  
473 because the error was calculated for mortars, for which the evaluation error is larger (Schoefs et  
474 al., 2023).

475 Therefore, in accordance with the previously stated modeling assumptions, we consider the  
476 measurement error to be negligible and retain model  $b$  for the SCAP-1D trajectory study.

#### 477 **6.4. Model $b$ : Parameter estimation, hypothesis testing and analysis (Steps II, III, IV)**

478 *Preliminary note: Since the RF considered in model  $b$  is log-normal, the data considered for the*  
479 *SCAP-1D implementation are the logarithms of the debiased data to consider a normal joint PDF.*

480 *The estimators of  $m_{LN}$ ,  $\sigma_{LN}^2$  and  $r_{95,LN}$  are then calculated from Equations (7) to (9) and from the*  
481 *estimators  $\hat{s}$ ,  $\hat{t}$  and  $\hat{\sigma}$ .*

482 Table 3 in the Appendix shows the result of the SCAP-1D implementation considering model  $b$ . Only  
483 the results of the  $\Sigma_{mod}$ -tests are considered due to the small number of points per trajectory. The  
484 analysis shows that the estimates for trajectories 3, 4, 5, and 16 are rejected due to the rejection of the

---

<sup>5</sup> some values are missing due to the singularity of the Fisher matrix

485 stationarity hypothesis by the KPSS-test. A model of the mean and covariance function that satisfies  
486 the hypothesis cannot be found, so no geostatistical parameter estimates are available for these  
487 trajectories. 77% of the estimates are then valid on **the** Ext side (10/13) and 92% on **the** Int side  
488 (11/12).

489 The estimates  $\hat{m}_{LN}$  and  $\hat{\sigma}_{LN}$  of the means and standard deviations are plotted with their confidence  
490 intervals (CIs) for each trajectory in Figure 15. Note that the estimates are consistent with the  
491 statistical mean and standard deviation profiles previously plotted in Figure 8. **Meanwhile, the**  
492 estimates  $\hat{r}_{95,LN}$  of the practical ranges are plotted with their CIs in Figure 16.

493 In the case of the trajectories associated with the Ext side, only 8 out of 10 estimates retained by  
494 SCAP-1D (i.e., 47% of all estimates) are finally retained after filtering out the outliers. These  
495 estimates all **satisfy** the interpretability criterion (see 4.1.5) with values between **100 and 300 cm** for  
496 a minimum measurement step of 30 cm. **However, contrary** to the assumptions made at the beginning  
497 of the study, there is no trend in the evolution of  $\hat{r}_{95,LN}$  as a function of the depth.

498 In the case of the trajectories associated with the Int side, all the estimates retained by SCAP-1D can  
499 be considered after filtering out the outliers (i.e., 92% of all the estimates). In accordance with the  
500 hypotheses formulated at the beginning of the study, we observe a **practical range of zero** near the  
501 surface, then a quasi-constant value around 60 cm-**100 cm** from 20 mm depth, respecting the  
502 interpretability criterion. This tendency reflects a transition from a purely random quantity of interest  
503 (**QI**) at the surface to a spatially correlated **QI**. at depth. We propose **the** following explanation:

- 504 • At the surface, many **spatiotemporally** random material (**microcracks**, ...), **physicochemical** (local  
505 runoff, ...), and environmental phenomena (biofouling, ...) contribute to the supply and  
506 convection of chlorides, so that, in coherence with the central limit theorem, the **chloride**  
507 **concentration** at the surface can be considered **completely** random, at least at the scale of the 30  
508 cm spatial discretization studied;
- 509 • at depth, the phenomenon of diffusion and fixation of  $C$  gradually takes precedence over their  
510 distribution within the coating, so that the fixation and diffusion properties of the concrete become

511 predominant with respect to the external and surface phenomena. Since the concrete has a certain  
512 spatial homogeneity, it is then consistent that  $C$  is spatially correlated.  
513 Furthermore, it is noted that the value of  $\hat{r}_{95,LN}$  at the rebar depth is of the same order as the as the  
514 conventional spacing of the vibrations during concrete pouring, from 30 to 60 cm (Guiraud, 2018;  
515 SETRA, 2005, p. 199). This observation then reinforces the idea that the spatial correlation of  $C$  is  
516 strongly related to the homogeneity properties of the concrete.

### 517 **6.5. Model b: construction of a unique autocorrelation model of chloride content**

518 The results obtained from the study of the Int side trajectories are much more convincing than those  
519 obtained from the study of the Ext side trajectories. In order to propose a unique autocorrelation  
520 model of  $C$  for the diffusion region, we then perform an MLE on the set of reduced centered  
521 trajectories of the Int side (without the first 10 mm), considering a unique scaling parameter  $a$ . Due  
522 to the non-stationarity of the mean and variance of  $C$  as a function of depth, we consider the  
523 trajectories independent of each other (we therefore neglect the SV along the  $z$ -axis). Still considering  
524 an exponential covariance model, the estimated practical range is  $\hat{r}_{95} = 71$  cm, i.e.  $\hat{a} = 24$  cm.  
525 We then state that the Gaussian model of identical practical range has the scale parameter  $\hat{a} = 41$  cm.  
526 However, the calculation of the ER from the AICC does not allow us to distinguish between the two  
527 models from the data, either by considering each trajectory or by estimating the MLE over all  
528 trajectories. In fact, their values are between 1 and 1.29. They are reported in Table 4 in the Appendix.  
529 Considering only the estimation results from the Int side, which are considered more robust due to  
530 the larger amount of data per trajectory, we can partially answer the questions raised in the  
531 introduction of this study. The SV of the chloride content seems indeed to depend on the depth, with  
532 a large variability within the convection zone, and much less and more stable in the diffusion zone  
533 with a practical range of about 70 cm. However, this value is more than two to three times lower  
534 than the practical range values of the average diffusion parameters  $C_{sa}$  and  $D_a$  reported in the  
535 literature, between 176 and 264 cm (Engelund & Sørensen, 1998; Karimi, 2002; O'Connor &

536 Kenshel, 2013). However, **it should be noted** that the latter are obtained with less robust methods than  
537 SCAP-1D and with even smaller **data** sets.

538 **However, the** question of the influence of **the** exposure conditions on the SV of **the** chloride content  
539 remains open **due to** the inconsistency of the practical range estimates on the Ext side. **However,**  
540 given the interpretation of the results for the Int side, it can be expected **to have** an influence only  
541 near the surface, **where** the chloride contents are already spatially decorrelated. However, this  
542 **suggestion** needs to be confirmed by studying an even richer database in order to increase the  
543 robustness of the estimates.

## 544 **7. Spatial variability estimation of chloride diffusion parameters of J-beam and physical** 545 **analysis**

### 546 **7.1. Geostatistical pre-study and choice of procedure parameters (Step I):**

547 The trajectories of  $\log(C_{sa})$  and  $\log(D_a)$  are shown in Figure 17 to Figure 20, as well as their  
548 means and the histograms and experimental semivariograms of centered trajectories. These curves  
549 are plotted for each trajectory in three cases: (i) stationary mean (no changepoint); (ii) piecewise  
550 stationary mean with one changepoint determined via the PELT algorithm (Killick et al., 2012);  
551 (iii) piecewise stationary average at two changepoints determined via the PELT algorithm.

552 The presence of sills on the experimental semi-variograms allows identifying the *a priori*  
553 stationary centered trajectories and thus the most appropriate non-stationarity model for each.

554 The shapes of the histograms and semi-variograms (nugget effect, tangent to the origin, ...)   
555 allows identifying models of joint density and a priori autocorrelation function that are adequate  
556 to the geostatistical description of the data.

557 Since the amount of data per trajectory is limited, especially for the Ext side, Step I could only  
558 be executed for the trajectories  $\log(C_{sa}) \geq 1$  and  $\log(D_a) \geq 1$ . The observations made as well as the  
559 models considered *a priori* are presented in Table 7.

560 7.1.1. *Fields models*

561 Although the histogram of the centered trajectory  $\log(C_{sa})_1$  is asymmetric, this may be due to  
562 the spatial correlation of the data. The histogram of  $\log(D_a)_1$  is centered. Moreover, we do not  
563 notice any nugget effect. This is due to the fact that the measurement noise of the chloride data is  
564 negligible (see 6.3). For simplicity and consistency with the results of the literature, a Gaussian  
565 Random Field model (GRF) is used to estimate spatial variability. This model is also retained by  
566 default for the  $\log(C_{sa})_2$  and  $\log(D_a)_2$  trajectories.

567 7.1.2. *Averaging models: apparent non-stationarity*

568 The trajectories are *a priori* globally stationary since the experimental semi-variograms without any  
569 changepoint in the mean present a sill. A constant mean model is therefore retained.

570 7.1.3. *Covariance function models*

571 Due to the large between measurement points, the spatial resolution is insufficient to visualize the  
572 presence of a tangent at the origin of the experimental semi-variograms. We therefore retain both the  
573 Gaussian and exponential covariance models without *a priori* preference.

574 This choice does not allow accounting for the correlation between  $\log(C_{sa})$  and  $\log(D_a)$ , well  
575 identified by (Othmen et al., 2018) and which should be modeled via a cross-correlated Random Field  
576 (XRF) (Chilès & Delfiner, 2012, p. 332). It is however justified as XRF modelling requires additional  
577 parameters (cross-correlation coefficient and cross-scale parameter(s)) which leads to  
578 **overparameterization** and unsuccessful assessment attempts due to the limited amount of data<sup>6</sup>.

579 **7.2. Parameter estimation, hypothesis testing and analysis (Steps II, III and IV)**

580 SCAP-1D steps II and III are applied to the trajectories of  $\log(D_a)$  considering the models kept in  
581 7.1. This allows the most appropriate covariance model to be determined from the calculation of

---

<sup>6</sup> MLE on raw data and MLE on data enriched via Metropolis-Hastings sampling did not give satisfactory results

582 Evidence Ratios (ER). These are computed from the AICC. Table 8 shows the results of SCAP-1D  
583 execution by trajectory. The models are ranked by increasing value of their ER.

584 First no estimate is rejected by the hypothesis tests. The estimates computed from the exponential  
585 and Gaussian models are then consistent for each of the trajectories except for the trajectory  $\log(C_{sa})$   
586 2 (relative errors of respectively 21%, 63%, 9% and 21% between the practical ranges of the  
587 Gaussian model and those of the exponential model). Furthermore, the exponential and Gaussian  
588 covariance models cannot be distinguished from the ERs (maximum difference observed for the  
589  $\log(C_{sa})$  1 trajectory with a ratio of 1 for the Gaussian model and a ratio of 2.13 for the  
590 exponential model). However, the Gaussian model leads to smaller coefficients of variation of the  
591 geostatistical parameters (up to a factor of 2.5 for the scale parameter of trajectory  $\log(C_{sa})$  1).

592 Second, the majority of the practical range estimates do not meet the interpretability criterion (see  
593 4.1.5). All of the estimates of  $r_{95}$  made on the  $\log(D_a)$  trajectories as well as the estimate made on  
594 the  $\log(C_{sa})$  2 trajectories are indeed of the order of 30 cm, which is the minimum spacing  
595 between measurements.

596 Therefore, only the estimates made on the  $\log(C_{sa})$  1 trajectory are retained. The estimated practical  
597 range is indeed 50 to 63 cm depending on the chosen covariance model, exponential or Gaussian  
598 (i.e., a ratio  $r_{95}/L$  of 0.05 to 0.07). The latter can then be preferred *a priori* because of its minimal  
599 ER even if exponential model is close.

600 Thus, due to the too large spacing between measurement points compared to the hidden value of their  
601 practical range, the question of whether the SV of the scattering parameters is a function of the  
602 exposure conditions cannot be answered here.

603 Furthermore, the interpretable estimates of practical ranges differ significantly from the 100 to 200  
604 cm values estimated by (O'Connor & Kenshel, 2013) on a bridge exposed to chloride ion penetration.  
605 Such a difference can be explained by the fact that these authors significantly enriched their initial  
606 kriging database (number of points multiplied by 7) before producing their estimates, which may have  
607 influenced them significantly.

## 608 **8. Conclusion**

609 In this paper, a new database is proposed for analysis of the spatial variability of chloride ingress into  
610 concrete. A total of 460 measurements was available, belonging to 2 exposures zones: 12 trajectories  
611 of 21 points for each profile on the Internal side (sheltered from wetting-drying cycles) and 13  
612 trajectories of 16 points on the External side. This data base was used to analyze the spatial variability  
613 of (i) chloride content, (ii) parameters of a model of chloride diffusion. The analysis is performed on  
614 the basis of a complete framework (SCAP-1D) which raises, rigorously for the first time, questions  
615 of stationarity, marginal distribution and auto-correlation.

616 The application to the total chloride content data showed that:

- 617 • the measurement error on total chloride content is negligible for the estimation of their spatial  
618 variability;
- 619 • near the surface, spatio-temporally random physico-chemical and environmental phenomena  
620 contribute to the diffusion and convection of chlorides so that, in coherence with the central limit  
621 theorem, total chloride content at the surface can be considered totally random;
- 622 • in depth (from about 20 mm), total chlorides diffusion and fixation gradually take precedence  
623 over their distribution within the coating, so that fixation and diffusion properties of concrete  
624 become predominant compared to the external and surface phenomena. Total chloride content is  
625 then spatially correlated with an estimated general practical range of 71 cm (scale parameter of  
626 24 cm) which is of the same order as the conventional vibration spacing during concrete pouring  
627 (30-60 cm (Guiraud, 2018; SETRA, 2005, p. 199)). This supports the fact that total chloride  
628 content spatial correlation in depth is strongly related to the homogeneity properties of the  
629 concrete resulting from pouring.

630 The application to the identification of diffusion parameters showed that:

631 The application to the chloride diffusion parameters data was presented in section 7. It allowed  
632 estimation of geostatistical parameters only for the logarithm of the average surface chlorides  
633 concentration. This is due to a limited number of points per trajectory (from 16 to 21) and a too large

634 spacing between measurement points (30 cm). The estimated practical range value is nevertheless  
635 consistent with that of the total chloride content in depth since it is between 50 and 63 cm.  
636 Implementation of SCAP-1D on these two datasets allowed to note that when the number of points  
637 per trajectory is limited but not small ( $\geq 20$ ), it is more efficient to first consider the results of  
638 statistical tests performed on the standardized trajectory from the empirical covariance matrix, and  
639 then in a second step those performed on the standardized trajectory from the modeled covariance  
640 matrix. This allows to first assess the validity of the mean model, then those of the marginal density  
641 model and the estimates of the geostatistical parameters of the source Random Field. On the contrary,  
642 when the number of points per trajectory is small ( $< 20$ ), it is preferable to consider only the results  
643 of the statistical tests performed on the standardized trajectory from the modeled covariance matrix,  
644 in order to guarantee its positivity of the latter.

645

646 **10. Appendix – Detailed tables of estimation process data**

647 *Table 1- Definition of trajectories and proportion of kriged data per trajectory – Ext side and Int side*

kriged data - Ex side				kriged data - Int side			
trajectory	depth (mm)	number	percentage	trajectory	depth (mm)	number	percentage
1	2.5	0	0%	16	2.5	0	0%
2	7.5	0	0%	17	7.5	1	5%
3	12.5	0	0%	18	12.5	1	5%
4	17.5	0	0%	19	17.5	1	5%
5	22.5	0	0%	20	22.5	2	10%
6	27.5	0	0%	21	27.5	1	5%
7	32.5	0	0%	22	32.5	2	10%
8	37.5	2	13%	23	37.5	2	10%
9	42.5	3	19%	24	42.5	4	19%
10	47.5	4	25%	25	47.5	3	14%
11	55	1	6%	26	55	4	19%
12	65	1	6%	27	65	4	19%
13	75	3	19%	28	75	9	43%
14	85	9	56%	29	85	15	71%
15	95	10	63%	30	95	17	81%
Total		33	14%	Total		66	21%

648 *Table 2 - Estimation of geostatistical parameters of total chloride concentration trajectories by SCAP-1D -*  
 649 *model a*

trajectory		model		Σexp-tests				Σmod-tests				estimates (data multiplied by k=10e4)					Coefficient of Variation (CoV)							
#	Side	z (mm)	Npts	model	cov	reg	chg	chi2	KS	KPSS	DF	chi2	KS	KPSS	DF	μ	s	t	a	r95	CoV μ	CoV s	CoV t	CoV a
1	Ext	2,5	16	GW	expon	0	0	0	0	0	1	0	0	0	1	18,66	19,63	0,00	0,01	0,03	NaN	NaN	NaN	NaN
2	Ext	7,5	16	GW	expon	0	0	0	0	0	1	0	0	0	1	25,86	64,36	0,00	0,00	0,00	2,0E-01	1,2E+00	5,7E-01	1,7E+00
3	Ext	12,5	16	GW	expon	0	0	1	0	1	0	0	0	0	1	40,04	49,27	36,47	2,57	6,28	1,2E-01	8,9E-01	5,3E-01	1,3E+00
4	Ext	17,5	16	GW	expon	0	0	0	0	0	1	0	0	1	1	41,59	91,14	0,00	0,01	0,01	5,7E-02	7,6E+02	1,8E+02	3,8E+05
5	Ext	22,5	16	GW	expon	0	0	0	0	1	0	0	0	1	1	39,44	96,31	0,00	0,01	0,01	NaN	NaN	NaN	NaN
6	Ext	27,5	16	GW	expon	0	0	1	0	0	1	0	0	0	1	36,65	53,47	0,00	0,52	1,55	NaN	NaN	NaN	NaN
7	Ext	32,5	16	GW	expon	0	0	1	0	0	1	0	0	0	1	34,95	59,57	0,00	0,32	0,96	NaN	NaN	NaN	NaN
8	Ext	37,5	16	GW	expon	0	0	0	0	0	1	0	0	0	1	30,95	62,31	0,00	0,37	1,12	NaN	NaN	NaN	NaN
9	Ext	42,5	16	GW	expon	0	0	0	0	0	1	0	0	0	1	29,20	18,89	7,15	2,17	5,80	9,1E-02	7,5E-01	7,5E-01	1,1E+00
10	Ext	47,5	16	GW	expon	0	0	0	0	0	1	0	0	0	1	27,69	19,49	0,00	0,71	2,12	NaN	NaN	NaN	NaN
11	Ext	55	16	GW	expon	0	0	0	0	0	1	0	0	0	1	20,98	16,46	0,00	0,01	0,02	NaN	NaN	NaN	NaN
12	Ext	65	16	GW	expon	0	0	1	1	1	0	0	0	0	1	18,89	11,95	0,00	0,01	0,03	4,6E-02	1,5E+02	9,6E+09	5,6E+05
13	Ext	75	16	GW	expon	0	0	0	0	0	1	0	0	0	1	18,61	8,47	0,00	0,01	0,03	3,9E-02	1,9E+02	9,0E+09	1,5E+05
14	Int	2,5	21	GW	expon	0	0	NaN	NaN	NaN	NaN	NaN	NaN	NaN	NaN	NaN	NaN	NaN	NaN	NaN	NaN	NaN	NaN	NaN
15	Int	7,5	21	GW	expon	0	0	0	0	0	1	0	0	0	1	22,94	135,81	0,00	0,00	0,00	NaN	NaN	NaN	NaN
16	Int	12,5	21	GW	expon	0	0	1	1	0	0	0	0	0	1	40,27	38,35	111,41	3,19	5,21	1,2E-01	1,3E+00	3,6E-01	1,5E+00
17	Int	17,5	21	GW	expon	0	0	0	0	0	1	0	0	0	1	53,50	180,15	0,00	0,00	0,00	NaN	NaN	NaN	NaN
18	Int	22,5	21	GW	expon	0	0	0	0	0	1	0	0	0	1	55,01	150,55	0,00	0,34	1,01	6,5E-02	1,1E+00	1,8E+07	1,0E+00
19	Int	27,5	21	GW	expon	0	0	0	0	0	1	0	0	0	1	50,09	154,45	0,00	0,24	0,72	6,5E-02	1,8E+00	3,2E+05	1,1E+00
20	Int	32,5	21	GW	expon	0	0	0	0	0	1	0	0	0	1	47,18	168,62	0,00	0,31	0,93	7,8E-02	9,9E-01	8,2E+07	8,8E-01
21	Int	37,5	21	GW	expon	0	0	0	0	0	1	0	0	0	1	39,46	126,85	4,31	0,09	0,26	6,4E-02	2,6E+01	7,8E+02	7,8E+00
22	Int	42,5	21	GW	expon	0	0	0	0	1	0	0	0	0	1	39,57	103,23	2,06	0,29	0,86	7,2E-02	1,2E+00	5,9E+01	1,1E+00
23	Int	47,5	21	GW	expon	0	0	1	0	0	1	0	0	0	1	34,59	72,53	0,00	0,35	1,06	7,3E-02	9,4E-01	2,7E+07	8,5E-01
24	Int	55	21	GW	expon	0	0	0	0	0	1	0	0	0	1	26,46	28,31	0,00	0,00	0,00	NaN	NaN	NaN	NaN
25	Int	65	21	GW	expon	0	0	0	0	0	1	0	0	0	1	24,73	25,35	0,00	0,25	0,74	5,4E-02	1,9E+00	6,9E+05	1,2E+00

GW : Gaussian + additive white noise; reg : regression degree of mean model; chg : maximum number of changepoints of mean model

651 *Table 3 - Estimation of geostatistical parameters of the logarithm of total chloride concentration trajectories*  
 652 *by SCAP-1D – model b*

trajectory				model			Σexp-tests				Σmod-tests				estimates (logarithm of data)			Coefficients of Variation (CoV)			
#	Face	z (mm)	Npts	modèle	cov	reg	chg	chi2	KS	KPSS	DF	chi2	KS	KPSS	DF	μ	s	a	CoV μ	CoV s	CoV a
1	Ext	2,5	16	G	expon	0	0	0	1	0	1	0	0	0	1	6,31	0,05	0,00	NaN	NaN	NaN
2	Ext	7,5	16	G	expon	0	0	0	1	1	1	0	0	0	1	6,04	0,08	0,52	1,6E-02	4,2E-01	7,5E-01
3	Ext	12,5	16	G	expon	0	0	0	0	0	1	0	0	1	1	5,54	0,06	0,26	1,3E-02	3,7E-01	8,4E-01
4	Ext	17,5	16	G	expon	0	0	0	0	0	1	0	0	1	1	5,51	0,05	0,00	1,0E-02	3,5E-01	1,8E+06
5	Ext	22,5	16	G	expon	0	0	0	0	1	1	0	0	1	1	5,57	0,07	0,13	1,2E-02	3,5E-01	1,6E+00
6	Ext	27,5	16	G	expon	0	0	0	0	1	1	0	0	0	1	5,63	0,05	0,47	1,3E-02	4,0E-01	6,4E-01
7	Ext	32,5	16	G	expon	0	0	0	1	1	1	0	0	0	1	5,68	0,05	0,25	1,1E-02	3,7E-01	9,4E-01
8	Ext	37,5	16	G	expon	0	0	0	0	0	1	0	0	0	1	5,81	0,06	0,40	1,4E-02	3,9E-01	6,7E-01
9	Ext	42,5	16	G	expon	0	0	0	1	1	0	0	0	0	1	5,86	0,03	0,93	1,3E-02	4,8E-01	6,5E-01
10	Ext	47,5	16	G	expon	0	0	0	1	1	1	0	0	0	1	5,90	0,03	0,69	1,1E-02	4,6E-01	7,2E-01
11	Ext	55	16	G	expon	0	0	0	0	0	1	0	0	0	1	6,19	0,05	0,02	8,7E-03	3,5E-01	4,8E+02
12	Ext	65	16	G	expon	0	0	0	0	0	1	0	0	0	1	6,29	0,04	0,01	NaN	NaN	NaN
13	Ext	75	16	G	expon	0	0	0	0	0	1	0	0	0	1	6,30	0,03	0,01	6,5E-03	3,5E-01	2,0E+05
14	Int	2,5	21	G	expon	0	0	0	0	0	1	0	0	0	1	6,18	0,05	0,00	NaN	NaN	NaN
15	Int	7,5	21	G	expon	0	0	0	0	0	1	0	0	0	1	6,19	0,21	0,00	NaN	NaN	NaN
16	Int	12,5	21	G	expon	0	0	0	0	0	1	0	0	1	1	5,58	0,14	0,01	1,5E-02	3,1E-01	1,5E+05
17	Int	17,5	21	G	expon	0	0	0	0	0	1	0	0	0	1	5,26	0,06	0,16	1,1E-02	3,1E-01	7,8E-01
18	Int	22,5	21	G	expon	0	0	0	1	0	1	0	0	0	1	5,23	0,05	0,34	1,2E-02	3,4E-01	5,3E-01
19	Int	27,5	21	G	expon	0	0	0	1	0	1	0	0	0	1	5,32	0,05	0,28	1,2E-02	3,3E-01	5,8E-01
20	Int	32,5	21	G	expon	0	0	0	1	0	1	0	0	0	1	5,39	0,06	0,28	1,3E-02	3,3E-01	6,0E-01
21	Int	37,5	21	G	expon	0	0	0	1	0	1	0	0	0	1	5,58	0,08	0,13	1,2E-02	3,1E-01	1,0E+00
22	Int	42,5	21	G	expon	0	0	0	0	0	1	0	0	0	1	5,57	0,07	0,28	1,3E-02	3,3E-01	5,7E-01
23	Int	47,5	21	G	expon	0	0	0	1	0	1	0	0	0	1	5,70	0,06	0,30	1,2E-02	3,3E-01	5,7E-01
24	Int	55	21	G	expon	0	0	0	0	0	1	0	0	0	1	5,95	0,04	0,19	7,9E-03	3,1E-01	6,4E-01
25	Int	65	21	G	expon	0	0	0	0	0	1	0	0	0	1	6,02	0,04	0,24	8,4E-03	3,2E-01	5,9E-01

G : Gaussian; reg : regression degree of mean model; chg : maximum number of changepoints of mean model

653

654 *Table 4 - Computation of the evidence ratios associated with the exponential and Gaussian covariance*  
 655 *models for model b using the corrected Akaike criterion*

trajectory				model			Corrected Akaike criteria		Evidence Ratios	
#	Face	z (mm)	Npts	model	reg	chg	cov gauss	cov expon	cov gauss	cov expon
17	Int	17,5	21	G	0	0	-3.21E+01	-3.22E+01	1.04	1.00
18	Int	22,5	21	G	0	0	-3.89E+01	-3.89E+01	1.00	1.05
19	Int	27,5	21	G	0	0	-3.59E+01	-3.55E+01	1.00	1.21
20	Int	32,5	21	G	0	0	-3.05E+01	-3.07E+01	1.11	1.00
21	Int	37,5	21	G	0	0	-2.39E+01	-2.39E+01	1.00	1.01
22	Int	42,5	21	G	0	0	-2.89E+01	-2.94E+01	1.29	1.00
23	Int	47,5	21	G	0	0	-3.14E+01	-3.18E+01	1.18	1.00
24	Int	55	21	G	0	0	-4.21E+01	-4.18E+01	1.00	1.14
25	Int	65	21	G	0	0	-4.22E+01	-4.18E+01	1.00	1.26

G : gaussian

656

657

658 **11. Data Availability Statement**

659 Some or all data, models, or code generated or used during the study are available from the  
660 corresponding author by request:

- 661 • chloride content dataset;
- 662 • whole MATLAB code generated during the study.

663 **12. Acknowledgment**

664 The authors would like to thank all the partners of iMAREO2 project: Keops Automation (D. Follut,  
665 D. Olivier), Université de Nantes (M. Roche), Nantes – Saint-Nazaire Port (P. Lijour, M. Labegorre).

666 The authors would like to thank the Pays de la Loire region for its financial support.

667 **13. References**

- 668 Angst, U., Elsener, B., Larsen, C. K., & Vennesland, Ø. (2009). Critical chloride content in  
669 reinforced concrete—A review. *Cement and Concrete Research*, 39(12), 1122–1138.  
670 <https://doi.org/10.1016/j.cemconres.2009.08.006>
- 671 Arnaud, M., & Emery, X. (2000). *Estimation et interpolation spatiale: Méthodes déterministes et*  
672 *méthodes géostatistiques*. Hermès. <http://agritrop.cirad.fr/487412/>
- 673 Baillargeon, S. (2005). *Le Krigeage*. Faculté des sciences et de génie UNIVERSITÉ LAVAL  
674 QUÉBEC. [https://archimede.mat.ulaval.ca/theses/S-Baillargeon\\_05.pdf](https://archimede.mat.ulaval.ca/theses/S-Baillargeon_05.pdf)
- 675 Bastidas-Arteaga, E., & Schoefs, F. (2015). Sustainable maintenance and repair of RC coastal  
676 structures. *Proceedings of the ICE-Maritime Engineering*, 168(4), 162–173.
- 677 Biondi, L., Perry, M., McAlorum, J., Vlachakis, C., Hamilton, A., & Lo, G. (2021). Alkali-  
678 Activated Cement Sensors for Sodium Chloride Monitoring. *IEEE Sensors Journal*, 21(19),  
679 21197–21204. <https://doi.org/10.1109/JSEN.2021.3100582>
- 680 Bonnet, S., Schoefs, F., & Salta, M. (2017). Sources of uncertainties for total chloride profile  
681 measurements in concrete: Quantization and impact on probability assessment of corrosion  
682 initiation. *European Journal of Environmental and Civil Engineering*, 1–16.  
683 <https://doi.org/10.1080/19648189.2017.1375997>
- 684 Bourreau, L., Bouteiller, V., Schoefs, F., Gaillet, L., Thauvin, B., Schneider, J., & Naar, S. (2019).  
685 Uncertainty assessment of concrete electrical resistivity measurements on a coastal bridge.  
686 *Structure and Infrastructure Engineering*, 1–11.  
687 <https://doi.org/10.1080/15732479.2018.1557703>

688 Bourreau, L., Gaillet, L., Bouteiller, V., Schoefs, F., Thauvin, B., Schneider, J., & Naar, S. (2020).  
689 Spatial identification of exposure zones of concrete structures exposed to a marine  
690 environment with respect to reinforcement corrosion. *Structure and Infrastructure*  
691 *Engineering*, 16(2), 346–354. <https://doi.org/10.1080/15732479.2019.1655072>  
692 BS 6349-1:2000. (2000). *Maritime structures. Code of practice for general criteria* [Norme].  
693 <https://shop.bsigroup.com/ProductDetail/?pid=000000000030055558>  
694 Burnham, K. P., & Anderson, D. R. (2010). *Model selection and multimodel inference: A practical*  
695 *information-theoretic approach* (2. ed., [4. printing]). Springer.  
696 Chilès, J.-P., & Delfiner, P. (2012). *Geostatistics: Modeling spatial uncertainty* (2. ed). Wiley.  
697 Clerc, R. (2021). *Sur l'estimation de la variabilité spatiale des paramètres de corrosion et sa*  
698 *nécessité pour les plans de maintenance des ouvrages maritimes en béton armé* [These de  
699 doctorat, Nantes]. <https://www.theses.fr/fr/2021NANT4052>  
700 Clerc, R., Oumouni, M., & Schoefs, F. (2019). SCAP-1D: A Spatial Correlation Assessment  
701 Procedure from unidimensional discrete data. *Reliability Engineering & System Safety*, 191,  
702 106498. <https://doi.org/10.1016/j.ress.2019.106498>  
703 Cressie, N. A. C. (1993). *Statistics for spatial data* (Rev. ed). Wiley.  
704 Der Kiureghian, A., & Ke, J.-B. (1987). The stochastic finite element method in structural  
705 reliability. In Y. K. Lin, G. I. Schuëller, & P. Spanos (Eds.), *Stochastic Structural*  
706 *Mechanics* (pp. 84–109). Springer Berlin Heidelberg.  
707 Dickey, D. A., & Fuller, W. A. (1981). Likelihood Ratio Statistics for Autoregressive Time Series  
708 with a Unit Root. *Econometrica*, 49(4), 1057. <https://doi.org/10.2307/1912517>  
709 Englund, S., & Sørensen, J. D. (1998). A probabilistic model for chloride-ingress and initiation of  
710 corrosion in reinforced concrete structures. *Structural Safety*, 20(1), 69–89.  
711 Fares, M., Villain, G., Bonnet, S., Palma Lopes, S., Thauvin, B., & Thiery, M. (2018). Determining  
712 chloride content profiles in concrete using an electrical resistivity tomography device.  
713 *Cement and Concrete Composites*, 94, 315–326.  
714 <https://doi.org/10.1016/j.cemconcomp.2018.08.001>  
715 Glasser, F. P., Marchand, J., & Samson, E. (2008). Durability of concrete—Degradation phenomena  
716 involving detrimental chemical reactions. *Cement and Concrete Research*, 38(2), 226–246.  
717 <https://doi.org/10.1016/j.cemconres.2007.09.015>  
718 Gomez-Cardenas, C., Sbartai, Z. M., Balayssac, J. P., Garnier, V., & Breyse, D. (2015). New  
719 optimization algorithm for optimal spatial sampling during non-destructive testing of  
720 concrete structures. *Engineering Structures*, 88, 92–99.  
721 <https://doi.org/10.1016/j.engstruct.2015.01.014>

- 722 Guiraud, P. (2018, April). Vibration des bétons. *Infociments*.  
723 <https://www.infociments.fr/betons/vibration-des-betons>
- 724 Hill, R. (1963). Elastic properties of reinforced solids: Some theoretical principles. *Journal of the*  
725 *Mechanics and Physics of Solids*, 11(5), 357–372. [https://doi.org/10.1016/0022-](https://doi.org/10.1016/0022-5096(63)90036-X)  
726 5096(63)90036-X
- 727 Hunkeler, D. F., Ungricht, H., & Deillon, F. (2000). *Determination of the chloride content of*  
728 *concrete and execution of a Round Robin test in two steps* (VSS 546). Eidg. Departement für  
729 Umwelt, Verkehr, Energie und Kommunikation (UVEK), Bundesamt für Strassen.  
730 [https://www.tfb.ch/Htdocs/Files/v/8671.pdf/Publikationsliste/ChloridbestimmungRingversu](https://www.tfb.ch/Htdocs/Files/v/8671.pdf/Publikationsliste/ChloridbestimmungRingversuchBerichtVSSNr.5462000.pdf)  
731 [chBerichtVSSNr.5462000.pdf](https://www.tfb.ch/Htdocs/Files/v/8671.pdf/Publikationsliste/ChloridbestimmungRingversuchBerichtVSSNr.5462000.pdf)
- 732 Johnson, N. L., Balakrishnan, N., & Kotz, S. (1995). *Continuous univariate distributions. Vol.2*  
733 (2ed.). Wiley.
- 734 Karimi, A. R. (2002). *Probabilistic assessment of deterioration and strength of concrete bridge*  
735 *beams and slabs* [Imperial College London].  
736 <https://ethos.bl.uk/OrderDetails.do?uin=uk.bl.ethos.540519>
- 737 Kaushik, S. K., & Islam, S. (1995). Suitability of sea water for mixing structural concrete exposed  
738 to a marine environment. *Cement and Concrete Composites*, 17(3), 177–185.  
739 [https://doi.org/10.1016/0958-9465\(95\)00015-5](https://doi.org/10.1016/0958-9465(95)00015-5)
- 740 Killick, R., Fearnhead, P., & Eckley, I. A. (2012). Optimal Detection of Changepoints With a  
741 Linear Computational Cost. *Journal of the American Statistical Association*, 107(500),  
742 1590–1598. <https://doi.org/10.1080/01621459.2012.737745>
- 743 Kwiatkowski, D., Phillips, P. C. B., Schmidt, P., & Shin, Y. (1992). Testing the null hypothesis of  
744 stationarity against the alternative of a unit root: How sure are we that economic time series  
745 have a unit root? *Journal of Econometrics*, 54(1), 159–178. [https://doi.org/10.1016/0304-](https://doi.org/10.1016/0304-4076(92)90104-Y)  
746 4076(92)90104-Y
- 747 Lecieux, Y., Rozière, E., Gaillard, V., Lupi, C., Leduc, D., Priou, J., Guyard, R., Chevreuil, M., &  
748 Schoefs, F. (2019). Monitoring of a Reinforced Concrete Wharf Using Structural Health  
749 Monitoring System and Material Testing. *Journal of Marine Science and Engineering*, 7(4),  
750 84. <https://doi.org/10.3390/jmse7040084>
- 751 Lecieux, Y., Schoefs, F., Bonnet, S., Lecieux, T., & Lopes, S. P. (2015). Quantification and  
752 uncertainty analysis of a structural monitoring device: Detection of chloride in concrete  
753 using DC electrical resistivity measurement. *Nondestructive Testing and Evaluation*, 30(3),  
754 216–232. <https://doi.org/10.1080/10589759.2015.1029476>

755 O'Connor, A. J., & Kenshel, O. (2013). Experimental Evaluation of the Scale of Fluctuation for  
756 Spatial Variability Modeling of Chloride-Induced Reinforced Concrete Corrosion. *Journal*  
757 *of Bridge Engineering*, 18(1), 3–14. [https://doi.org/10.1061/\(ASCE\)BE.1943-5592.0000370](https://doi.org/10.1061/(ASCE)BE.1943-5592.0000370)

758 Othmen, I., Bonnet, S., & Schoefs, F. (2018). Statistical investigation of different analysis methods  
759 for chloride profiles within a real structure in a marine environment. *Ocean Engineering*,  
760 157, 96–107. <https://doi.org/10.1016/j.oceaneng.2018.03.040>

761 Oumouni, M., & Schoefs, F. (2021a). A Perturbed Markovian process with state-dependent  
762 increments and measurement uncertainty in degradation modeling. *Computer-Aided Civil*  
763 *and Infrastructure Engineering*, 36(8), 978–995. <https://doi.org/10.1111/mice.12644>

764 Oumouni, M., & Schoefs, F. (2021b). Spatial variability assessment of structures from adaptive  
765 NDT measurements. *Structural Safety*, 89, 102052.  
766 <https://doi.org/10.1016/j.strusafe.2020.102052>

767 Priou, J., Lecieux, Y., Chevreuil, M., Gaillard, V., Lupi, C., Leduc, D., Rozière, E., Guyard, R., &  
768 Schoefs, F. (2019). In situ DC electrical resistivity mapping performed in a reinforced  
769 concrete wharf using embedded sensors. *Construction and Building Materials*, 211, 244–  
770 260. <https://doi.org/10.1016/j.conbuildmat.2019.03.152>

771 Qu, F., Li, W., Dong, W., Tam, V. W. Y., & Yu, T. (2021). Durability deterioration of concrete  
772 under marine environment from material to structure: A critical review. *Journal of Building*  
773 *Engineering*, 35, 102074. <https://doi.org/10.1016/j.jobe.2020.102074>

774 Ragab, A. M., Elgammal, M. A., Hodhod, O. A., & Ahmed, T. E. (2016). Evaluation of field  
775 concrete deterioration under real conditions of seawater attack. *Construction and Building*  
776 *Materials*, 119, 130–144. <https://doi.org/10.1016/j.conbuildmat.2016.05.014>

777 Ravahatra, N. R., Duprat, F., Schoefs, F., de Larrard, T., & Bastidas-Arteaga, E. (2017). Assessing  
778 the Capability of Analytical Carbonation Models to Propagate Uncertainties and Spatial  
779 Variability of Reinforced Concrete Structures. *Frontiers in Built Environment*, 3.  
780 <https://doi.org/10.3389/fbuil.2017.00001>

781 Safhi, A. el M., Benzerzour, M., Rivard, P., Abriak, N.-E., & Ennahal, I. (2019). Development of  
782 self-compacting mortars based on treated marine sediments. *Journal of Building*  
783 *Engineering*, 22, 252–261. <https://doi.org/10.1016/j.jobe.2018.12.024>

784 Schoefs, F., Awa Zahui Raissa, K., Bonnet, S., & O'Conor, A. J. (2023). Uncertainty quantification  
785 of semi-destructive testing for chloride content assessment for a concrete bridge in maritime  
786 environment. *Frontiers in Built Environment*, 9.  
787 <https://www.frontiersin.org/articles/10.3389/fbuil.2023.1130066>

- 788 Schoefs, F., Bastidas-Arteaga, E., Tran, T. V., Villain, G., & Derobert, X. (2016). Characterization  
789 of random fields from NDT measurements: A two stages procedure. *Engineering Structures*,  
790 *111*, 312–322. <https://doi.org/10.1016/j.engstruct.2015.11.041>
- 791 Schoefs, F., Bastidas-Arteaga, E., & Tran, T.-V. (2017). Optimal embedded sensor placement for  
792 spatial variability assessment of stationary random fields. *Engineering Structures*, *152*, 35–  
793 44. <https://doi.org/10.1016/j.engstruct.2017.08.070>
- 794 Schoefs, F., Oumouni, M., Clerc, R., Othmen, I., & Bonnet, S. (2017). Statistical analysis and  
795 probabilistic modeling of chloride ingress spatial variability in concrete coastal  
796 infrastructures. *Edition 4, Split, Croatie*, 229–234. <https://doi.org/10.5150/cmcm.2017.042>
- 797 Schoefs, F., Oumouni, M., Follut, D., Lecieux, Y., Gaillard, V., Lupi, C., & Leduc, D. (2022).  
798 Added value of monitoring for the maintenance of a reinforced concrete wharf with spatial  
799 variability of chloride content: A practical implementation. *Structure and Infrastructure*  
800 *Engineering*, *0(0)*, 1–13. <https://doi.org/10.1080/15732479.2022.2077767>
- 801 SETRA. (2005). *Mémoar—Mémento pour la mise en oeuvre sur ouvrages d'art*. Cerema (ex-Setra).  
802 <https://www.cerema.fr/fr/centre-ressources/boutique/memoar-memento-mise-oeuvre->  
803 [ouvrages-art](https://www.cerema.fr/fr/centre-ressources/boutique/memoar-memento-mise-oeuvre-ouvrages-art)
- 804 Stewart, M. G. (2004). Spatial variability of pitting corrosion and its influence on structural fragility  
805 and reliability of RC beams in flexure. *Structural Safety*, *26(4)*, 453–470.  
806 <https://doi.org/10.1016/j.strusafe.2004.03.002>
- 807 Stewart, M. G., & Mullard, J. A. (2007). Spatial time-dependent reliability analysis of corrosion  
808 damage and the timing of first repair for RC structures. *Engineering Structures*, *29(7)*,  
809 1457–1464. <https://doi.org/10.1016/j.engstruct.2006.09.004>
- 810 Stewart, M. G., & Val, D. V. (2003). Multiple Limit States and Expected Failure Costs for  
811 Deteriorating Reinforced Concrete Bridges. *Journal of Bridge Engineering*, *8(6)*, 405–415.  
812 [https://doi.org/10.1061/\(ASCE\)1084-0702\(2003\)8:6\(405\)](https://doi.org/10.1061/(ASCE)1084-0702(2003)8:6(405))
- 813 Torres-Luque, M., Bastidas-Arteaga, E., Schoefs, F., Sánchez-Silva, M., & Osma, J. F. (2014).  
814 Non-destructive methods for measuring chloride ingress into concrete: State-of-the-art and  
815 future challenges. *Construction and Building Materials*, *68*, 68–81.
- 816 Torres-Luque, M., Osma, J. F., Sánchez-Silva, M., Bastidas-Arteaga, E., & Schoefs, F. (2017).  
817 Chlordetect: Commercial Calcium Aluminate Based Conductimetric Sensor for Chloride  
818 Presence Detection. *Sensors*, *17(9)*, 2099. <https://doi.org/10.3390/s17092099>
- 819 Vennesland, P. Ø., Climent, M. A., & Andrade, C. (2013). Recommendations of RILEM TC 178-  
820 TMC: Testing and modelling chloride penetration in concrete. *Materials and Structures*, *8*.  
821 <https://doi.org/10.1617/s11527-012-9968-1>

- 822 Wasserman, L. (2004). *All of Statistics*. Springer New York. <https://doi.org/10.1007/978-0-387->  
823 21736-9
- 824 Watanabe, A., Tokuda, S., Mizuta, Y., Miyamoto, S., Nakanishi, T., Furukawa, H., & Minagawa,  
825 H. (2021). Toward automated non-destructive diagnosis of chloride attack on concrete  
826 structures by near infrared spectroscopy. *Construction and Building Materials*, 305, 124796.  
827 <https://doi.org/10.1016/j.conbuildmat.2021.124796>
- 828 Wegian, F. M. (2010). Effect of seawater for mixing and curing on structural concrete. *The IES*  
829 *Journal Part A: Civil & Structural Engineering*, 3(4), 235–243.  
830 <https://doi.org/10.1080/19373260.2010.521048>
- 831 Zaki, A., Chai, H. K., Aggelis, D. G., & Alver, N. (2015). Non-Destructive Evaluation for  
832 Corrosion Monitoring in Concrete: A Review and Capability of Acoustic Emission  
833 Technique. *Sensors*, 15(8), Article 8. <https://doi.org/10.3390/s150819069>

834

835

836 **14. Embedded Tables**

837 *Table 5 - Exponential and Gaussian autocorrelation functions, and relations between their scale parameter,*  
 838 *fluctuation scale and practical range*

Name	Model	$\theta$	$\rho(h = \theta)$	$r_{95}$	$\rho(h = r_{95})$
exponential	$\rho(h) = \exp(-\ h\ /a)$	$2a$	0.135	$3a$	0.05
Gaussian	$\rho(h) = \exp(-\ h\ ^2/a)$	$\sqrt{\pi}a$	0.043	$1.73a$	0.05

$a$ : scale parameter;  $\theta$ : fluctuation parameter;  $r_{95}$ : practical range;  
 $\rho(\cdot)$ : autocorrelation function

839

840 *Table 6- Numbering of the trajectories of average scattering parameters (J-beam)*

trajectory	Side	number of measurement points
log ( $C_{sa}$ ) 1	Int	21
log ( $D_a$ ) 1	Int	21
log ( $C_{sa}$ ) 1	Ext	16
log ( $D_a$ ) 2	Ext	16

841

842 *Table 7- Geostatistical pre-study of the trajectories of the logarithms of the average diffusion parameters –*  
 843 *J-beam*

trajectory	analysis of experimental semi-variograms and histograms					models considered		
	chgpt(*)	nugget	oscillations	original tangent	histogram shape	average	field	covariance
log ( $C_{sa}$ ) 1	0	no	no	insufficient resolution	asymmetrical	cste	GRF	Gauss or expon
log ( $D_a$ ) 1	0	no	no	insufficient resolution	symmetrical	cste	GRF	Gauss or expon
log ( $C_{sa}$ ) 2	-	-	-	-	-	cste	GRF	Gauss or expon
log ( $D_a$ ) 2	-	-	-	-	-	cste	GRF	Gauss or expon

(\*) : changepoints necessary for the experimental semi-variogram to have a sill

844

845 *Table 8- Geostatistical parameter estimates of the trajectories of the logarithms of the mean scattering*  
 846 *parameters by SCAP-ID*

traj	model					$\Sigma_{exp}$ -tests				$\Sigma_{mod}$ -tests				estimates			CoV			model selection		range	
	#	model	cov	chg	reg	$\chi^2$	KS	KPSS	DF	$\chi^2$	KS	KPSS	DF	$\alpha 1$	s	a1 (cm)	$\alpha 1$	s	a1	AICc	ER	$r_{95}$ (cm)	$r_{95}/L$
log( $C_{sa}$ ) 1	1	GRF	expon	0	0	0	0	0	1	0	0	0	1	-4,82	0,13	17	0,02	0,31	0,81	-14,08	2,13	50	0,05
	2	GRF	gauss	0	0	0	0	0	1	0	0	0	1	-4,81	0,15	37	0,02	0,39	0,33	-15,59	1,00	63	0,07
log( $C_{sa}$ ) 2	1	GRF	expon	0	0	0	0	0	1	0	0	0	1	-5,20	0,07	19	0,01	0,36	1,20	-19,22	1,00	57	0,06
	2	GRF	gauss	0	0	0	0	0	1	0	0	0	1	-5,20	0,07	20	0,01	0,36	0,80	-19,11	1,06	35	0,04
log( $D_a$ ) 1	1	GRF	expon	0	0	0	0	0	1	0	0	0	1	-27,48	0,31	10	0,00	0,31	1,65	3,78	1,01	29	0,03
	2	GRF	gauss	0	0	0	0	0	1	0	0	0	1	-27,48	0,31	18	0,00	0,31	0,77	3,76	1,00	32	0,03
log( $D_a$ ) 2	1	GRF	expon	0	0	0	0	0	1	0	0	0	1	-27,56	0,29	13	0,01	0,35	1,40	4,19	1,00	40	0,04
	2	GRF	gauss	0	0	0	0	0	1	0	0	0	1	-27,56	0,29	19	0,01	0,35	0,72	4,21	1,01	33	0,04

847

848

849 **15. List of Figure Captions**

850 Figure 1 - Illustration of the geostatistical formalism: GRF  $Y$

851 Figure 2 - Illustration of the geostatistical formalism: noisy GRF  $Z$

852 Figure 3 - General flowchart of SCAP-1D

853 Figure 4 - Interpretability of practical range (Gaussian autocorrelograms  $\rho(h)$  with three practical  
854 range values, measurement step  $\Delta x = 5$ )

855 Figure 5 - Size and position of rebars of the “J-beam” (distance unit: cm; diameter unit: mm)

856 Figure 6 - Different views: a) Aerial view, b) Sketch of bridge 3, 4 and 5, c) Beam J, d) Exposed  
857 (Ext) and sheltered (Int) side of beam J.

858 Figure 7 - Samples taken for chloride titration (J-beam): a) Locations, b) Cross-section, c) Slices

859 Figure 8- Profiles of the evolution of the statistical mean and standard deviation of total chloride  
860 concentrations according to the depth of embedding

861 Figure 9 - Total chloride concentration database and illustration of the principle of implementing  
862 SCAP-1D on total chloride concentration data

863 Figure 10 - Trajectories and statistical averages of the logarithms of the mean diffusion parameters  
864 at 28 years (J-beam)

865 Figure 11 - Raw trajectories and associated statistical means - trajectory number / depth  
866 correspondences presented in Table 5

867 Figure 12 - Selected trajectories and associated statistical means

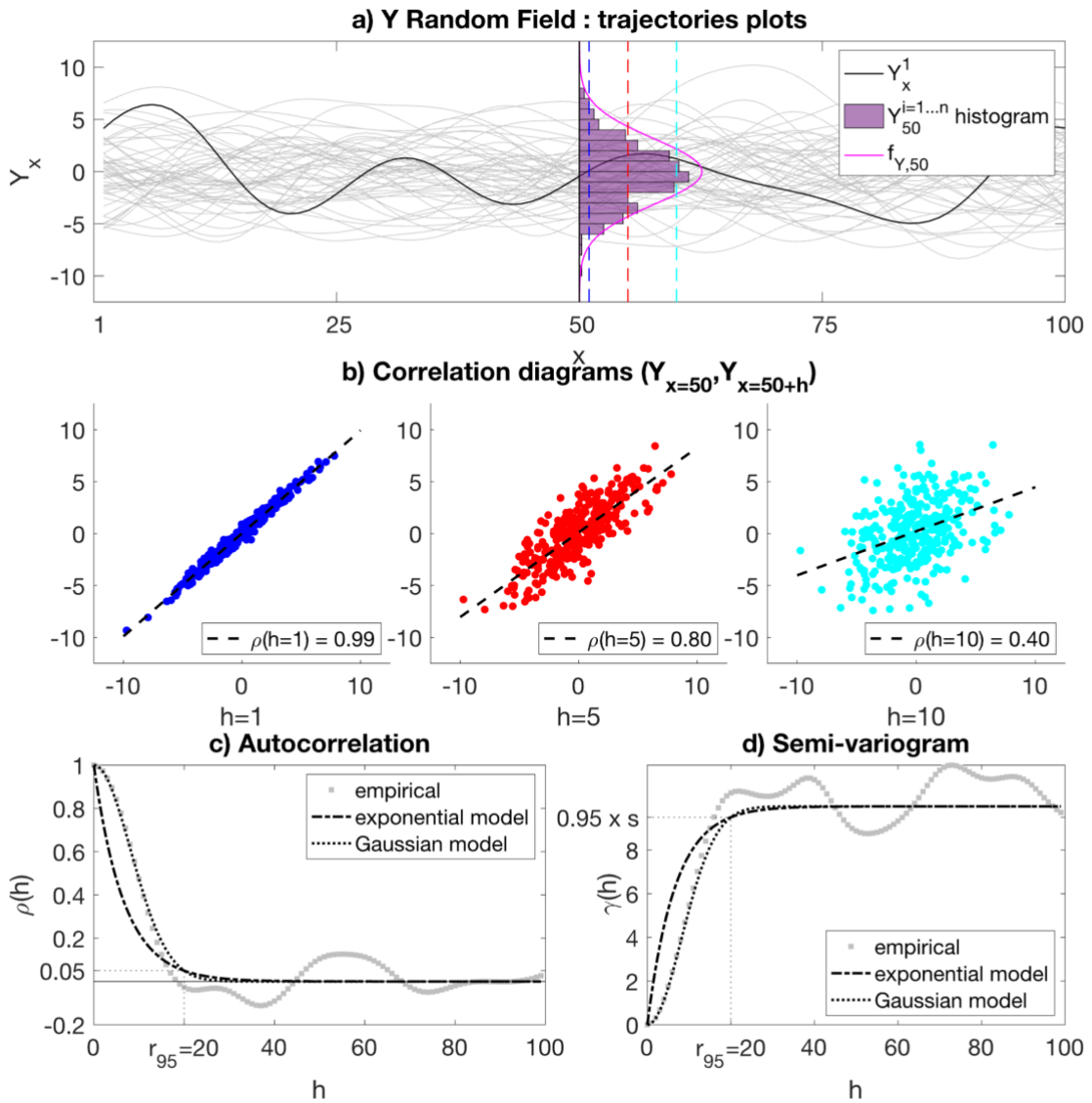
868 Figure 13 - Profiles of the evolution of the mean and standard deviation of total chloride content  
869 according to the depth - model a

870 Figure 14 - Study of the Signal to Noise Ratio - model a

871 Figure 15 - Profiles of the evolution of the mean and standard deviation of total chloride  
872 concentrations according to the depth of embedding - model b

873 Figure 16 - Practical range profiles of total chloride concentration trajectories as a function of  
874 embedment depth - model b

875 Figure 17- Data and averages of trajectory 1 of log mean surface concentration; histograms of  
876 trajectories so centered; experimental semivariograms of trajectories so centered  
877 Figure 18- Data and averages of trajectory 1 of logarithm of mean diffusivity; histograms of  
878 trajectories so centered; experimental semivariograms of trajectories so centered  
879 Figure 19- Data and averages of logarithm of mean surface concentration trajectory 2; histograms of  
880 trajectories so centered; experimental semivariograms of trajectories so centered  
881 Figure 20- Data and averages of trajectory 2 of logarithm of mean diffusivity; histograms of  
882 trajectories so centered; experimental semivariograms of trajectories so centered  
  
883  
884

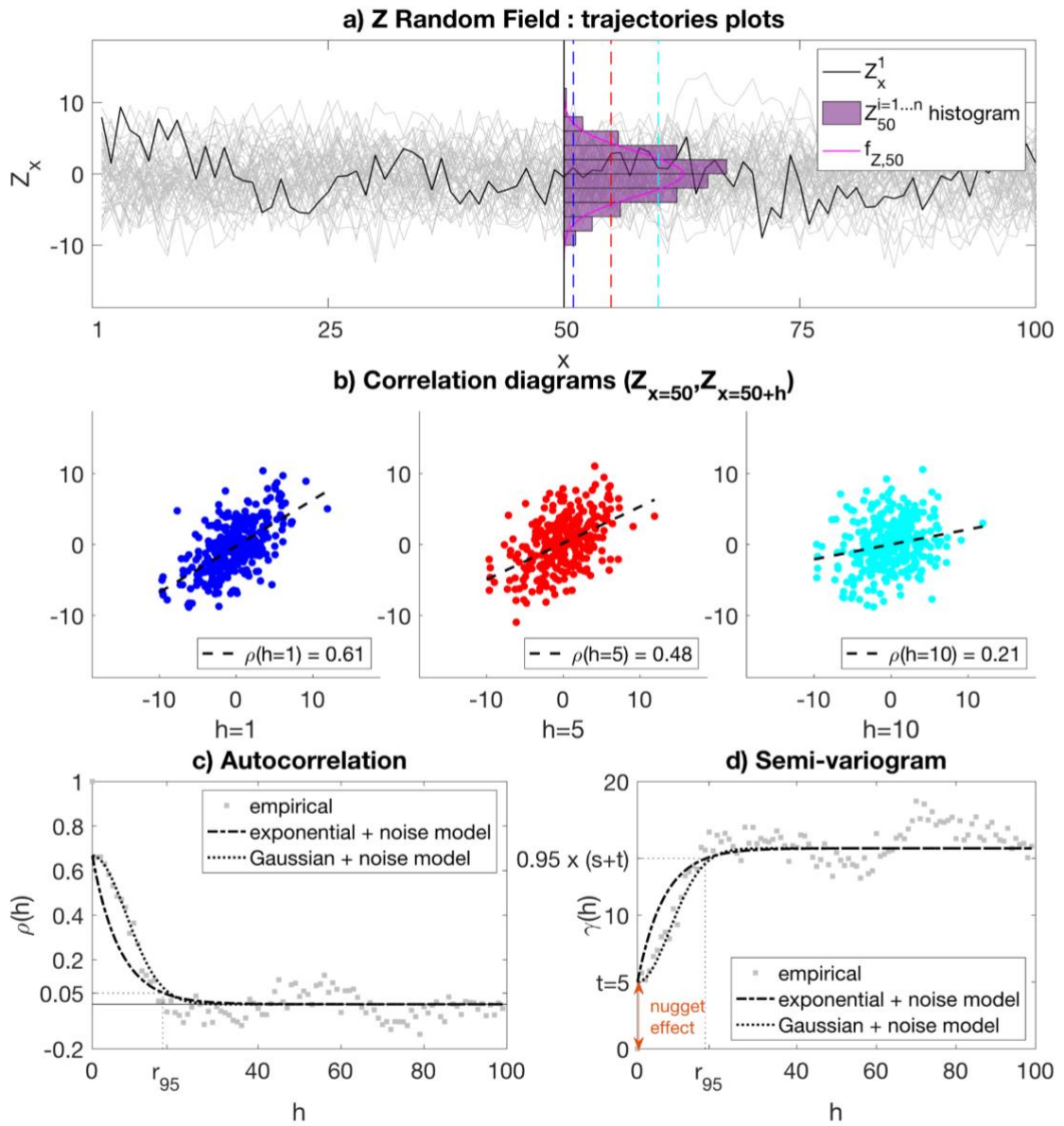


885

886

Figure 1 - Illustration of the geostatistical formalism: GRF  $Y$

887

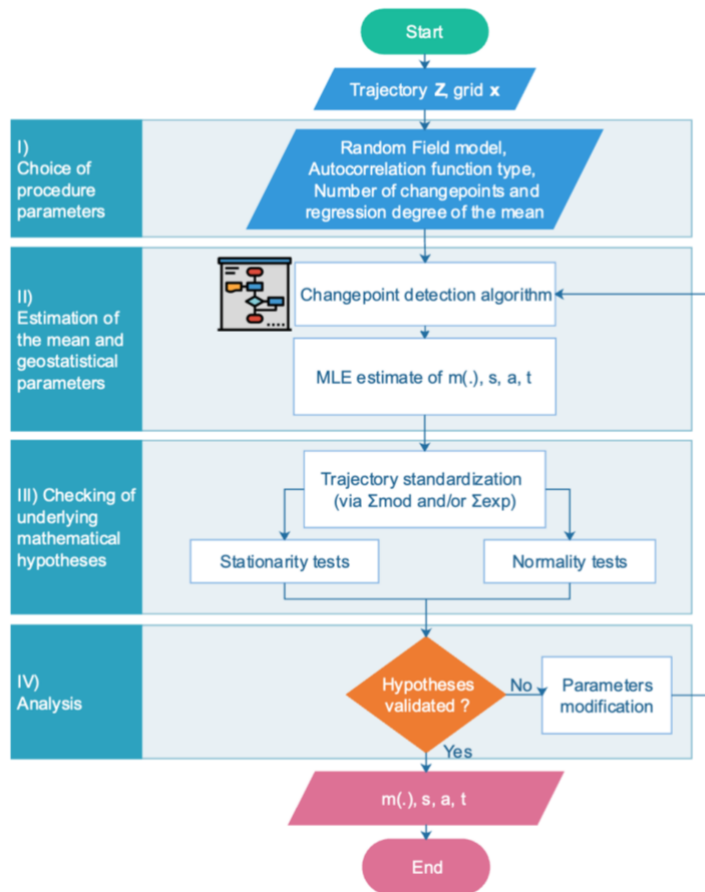


888

889

Figure 2 - Illustration of the geostatistical formalism: noisy GRF Z

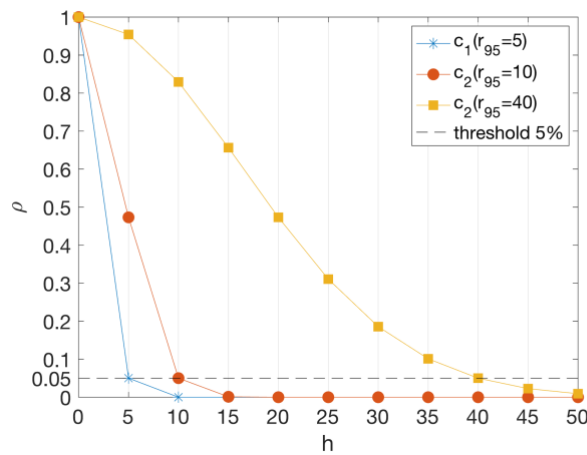
890



891

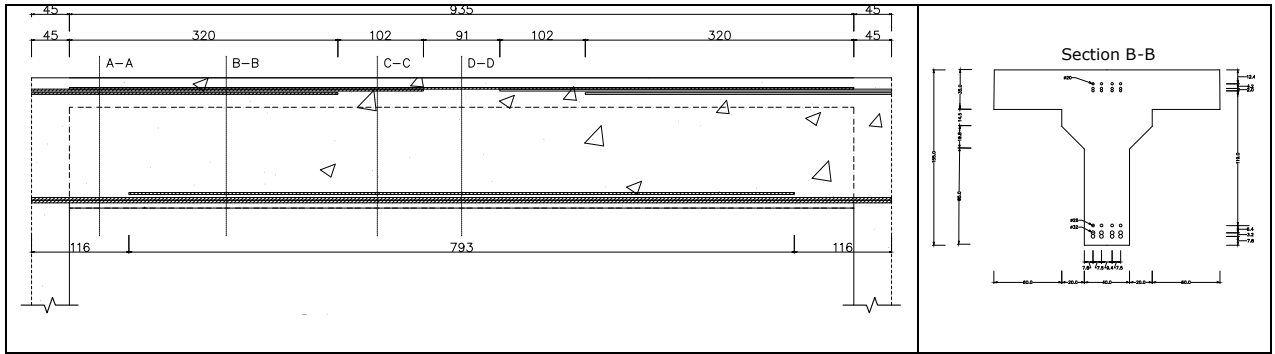
892

Figure 3 - General flowchart of SCAP-1D



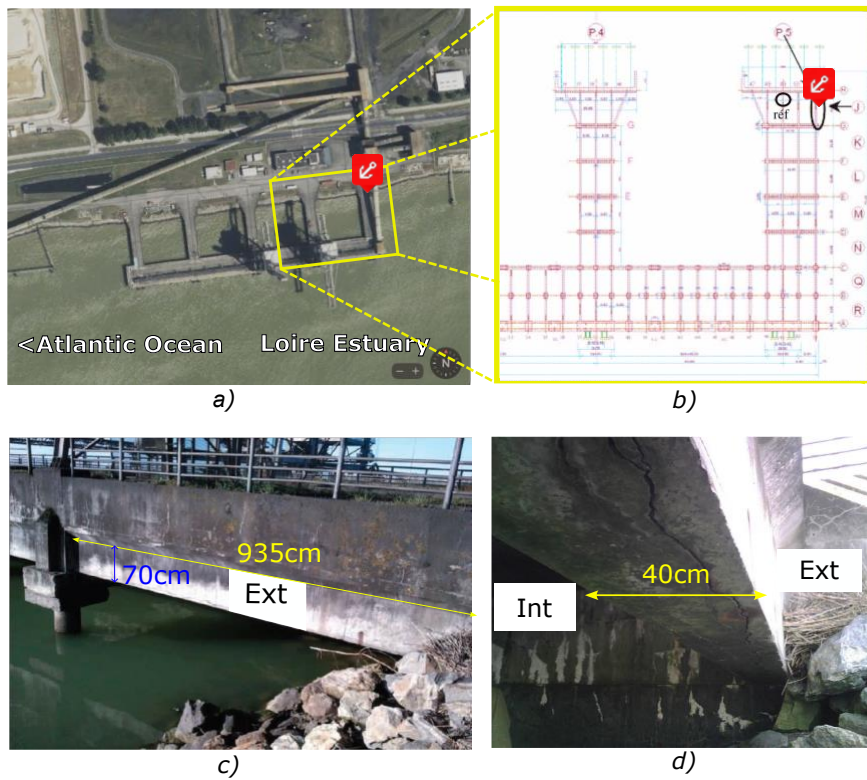
893

894 Figure 4 - Interpretability of practical range (Gaussian autocorrelograms  $\rho(h)$  with three practical range  
895 values, measurement step  $\Delta x = 5$ )



896 *Figure 5 - Size and position of rebars of the “J-beam” (distance unit: cm; diameter unit: mm)*

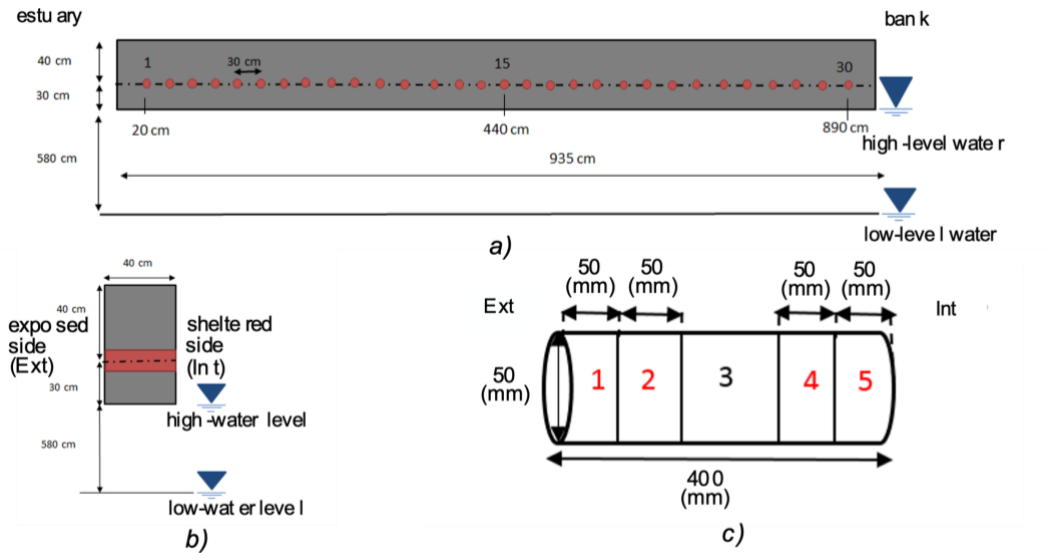
897



898

899 *Figure 6 - Different views: a) Aerial view, b) Sketch of bridge 3, 4 and 5, c) Beam J, d) Exposed (Ext) and*  
 900 *sheltered (Int) side of beam J.*

901

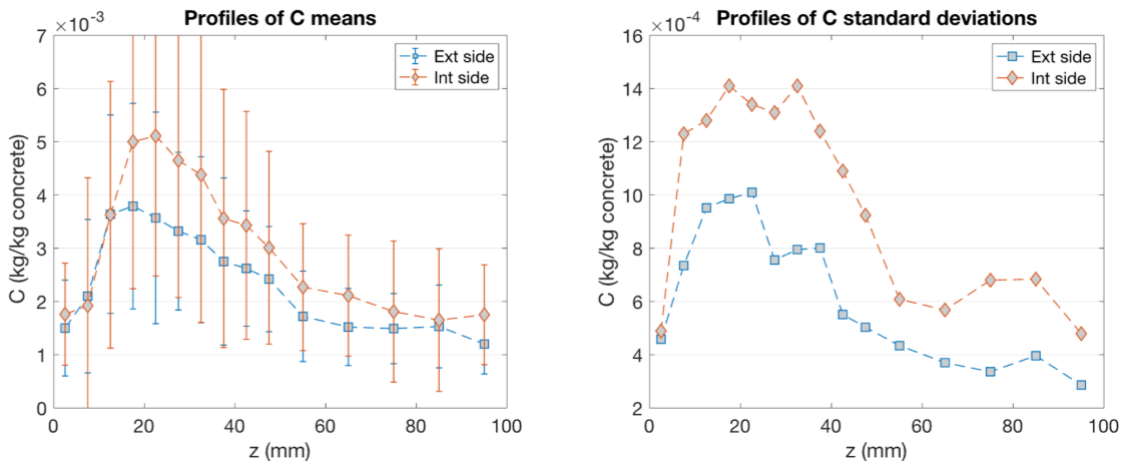


902

903

Figure 7 - Samples taken for chloride titration (J-beam): a) Locations, b) Cross-section, c) Slices

904

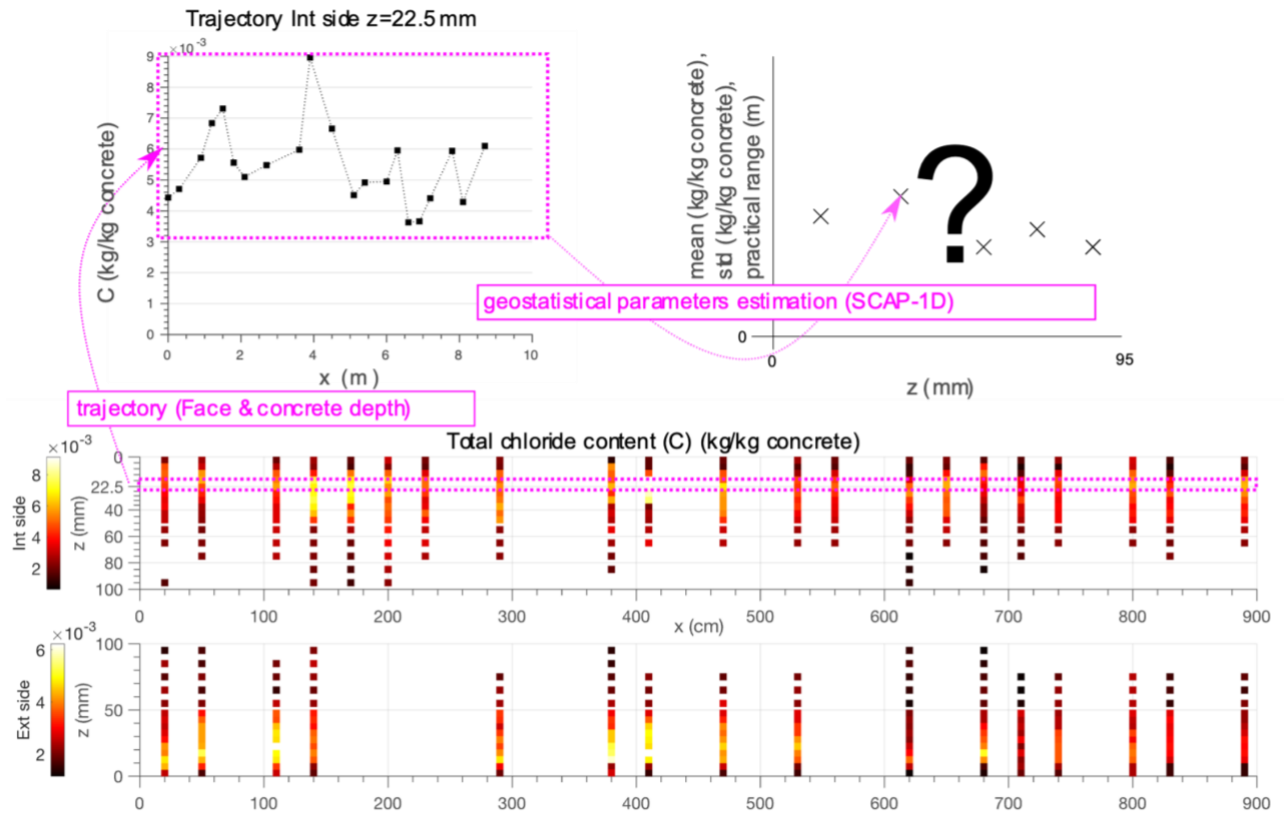


905

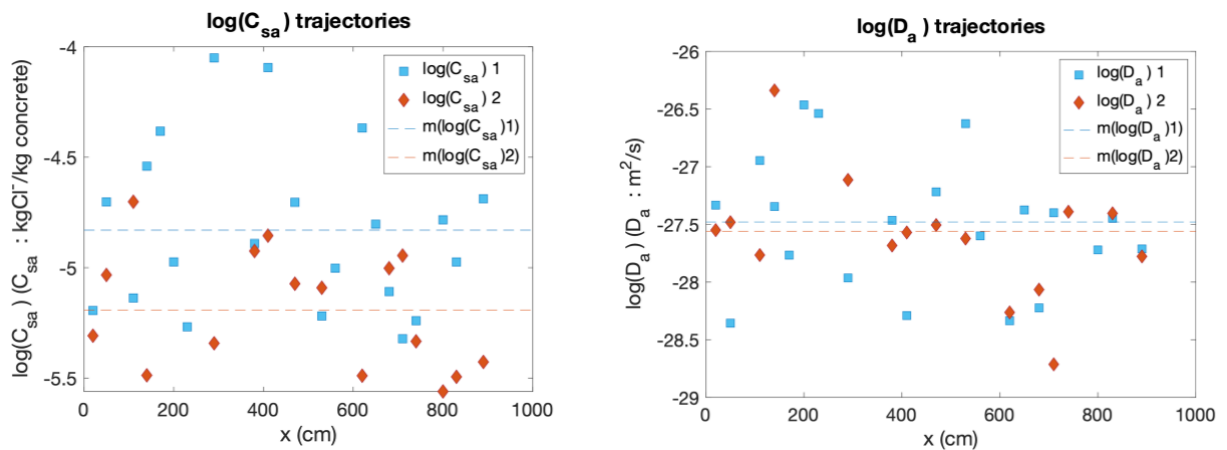
906

Figure 8- Profiles of the evolution of the statistical mean and standard deviation of total chloride concentrations according to the depth of embedding

908



909  
 910 *Figure 9 - Total chloride concentration database and illustration of the principle of implementing SCAP-1D*  
 911 *on total chloride concentration data*

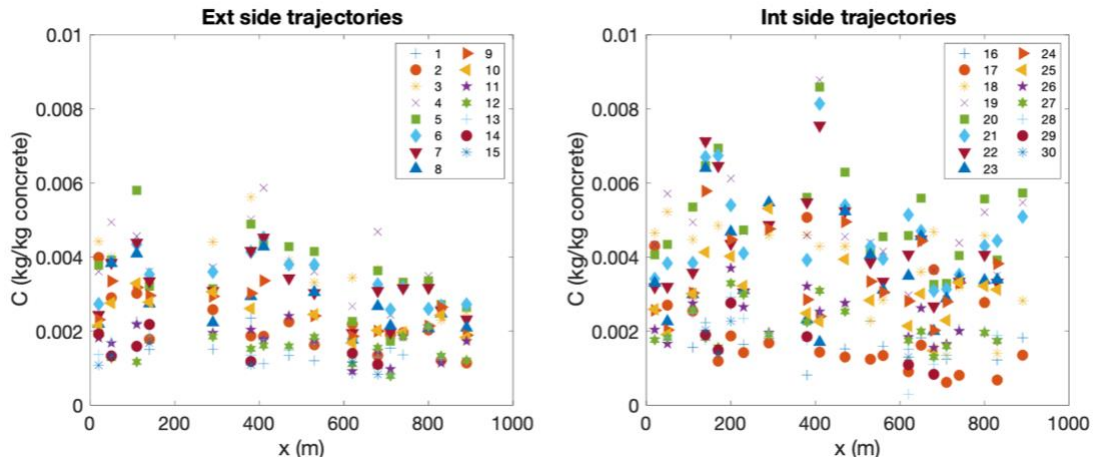


(a) Trajectories and statistical averages of the logarithms of the 28-year average surface concentrations of total chlorides - beam J

(b) trajectories and statistical means of the logarithms of the mean diffusivities of total chlorides at 28 years - beam J

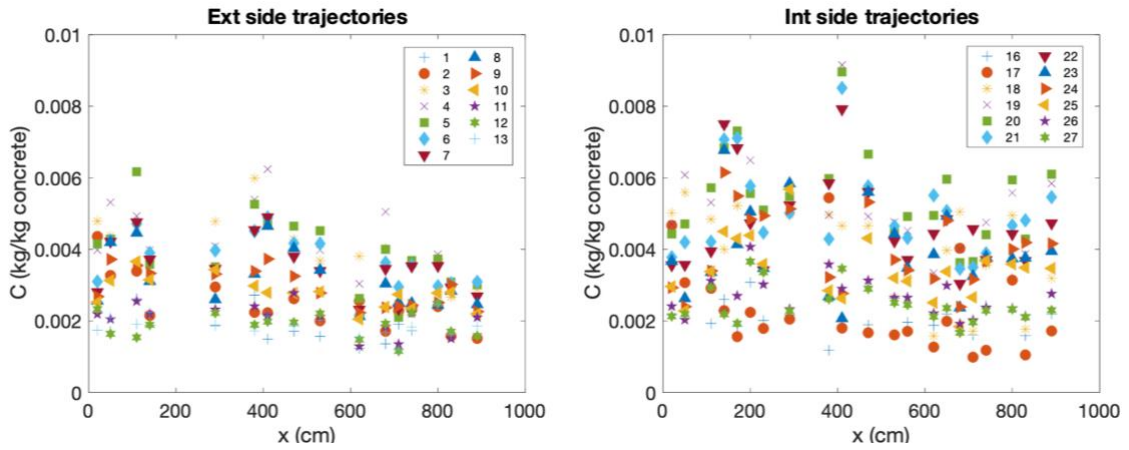
912 *Figure 10 - Trajectories and statistical averages of the logarithms of the mean diffusion parameters at 28*  
 913 *years (J-beam)*

914



915  
 916 *Figure 11 - Raw trajectories and associated statistical means - trajectory number / depth correspondences*  
 917 *presented in Table 1*

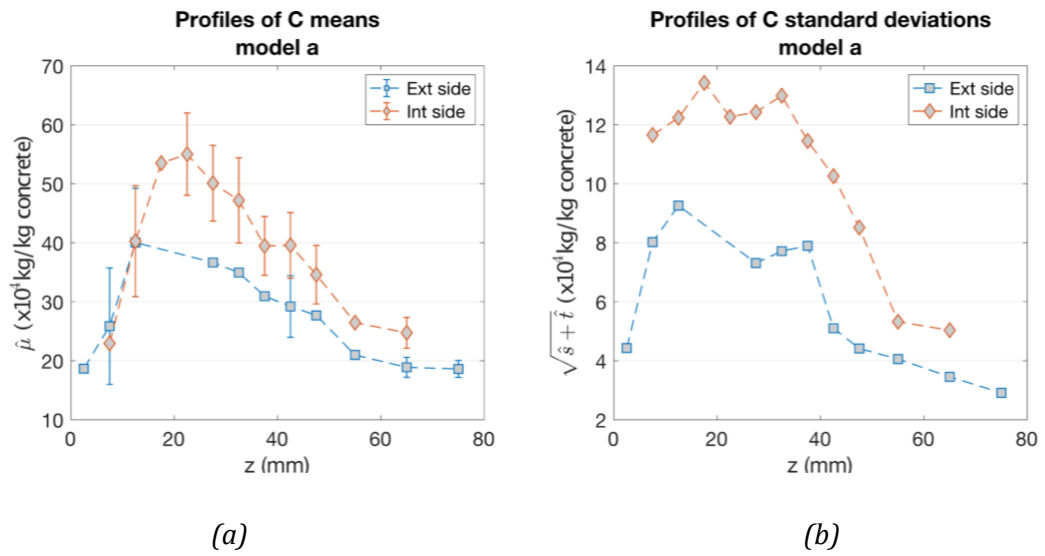
918



919  
 920 *Figure 12 - Selected trajectories and associated statistical means*

921

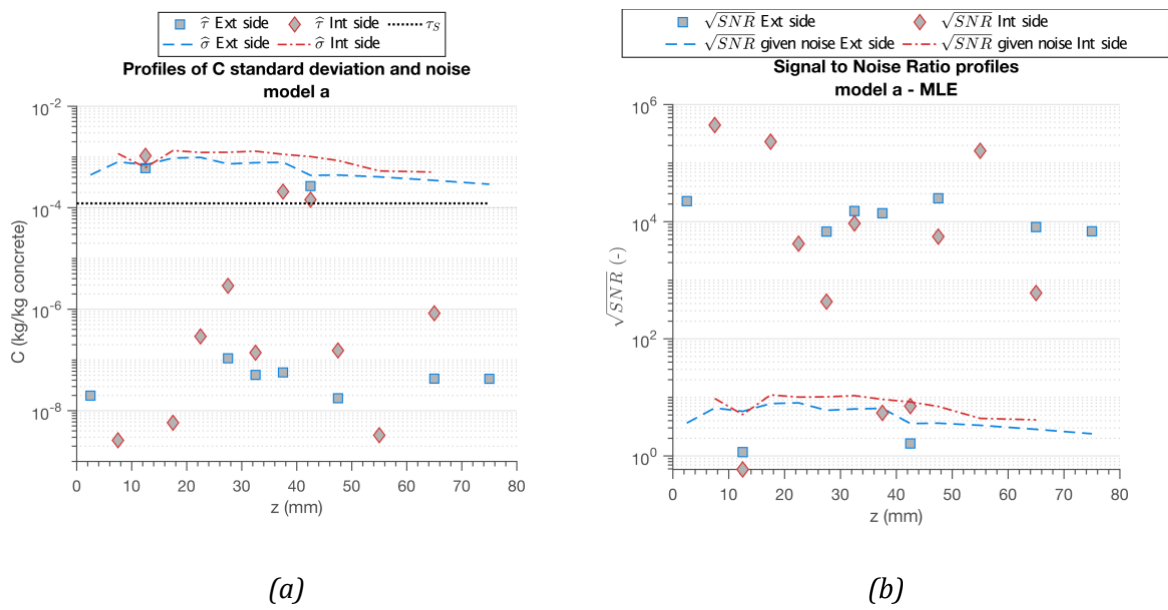
922



923

924 Figure 13 - Profiles of the evolution of the mean and standard deviation of total chloride content according  
925 to the depth - model a

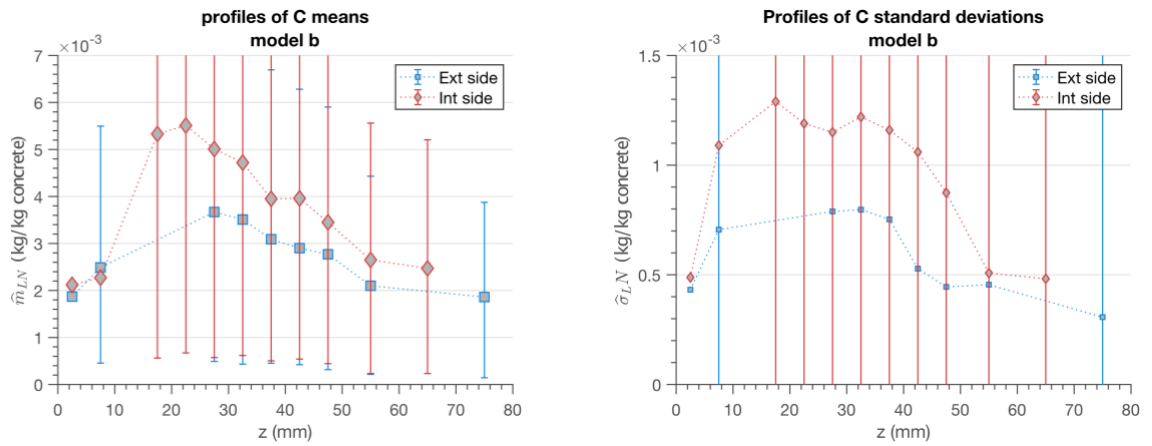
926



927

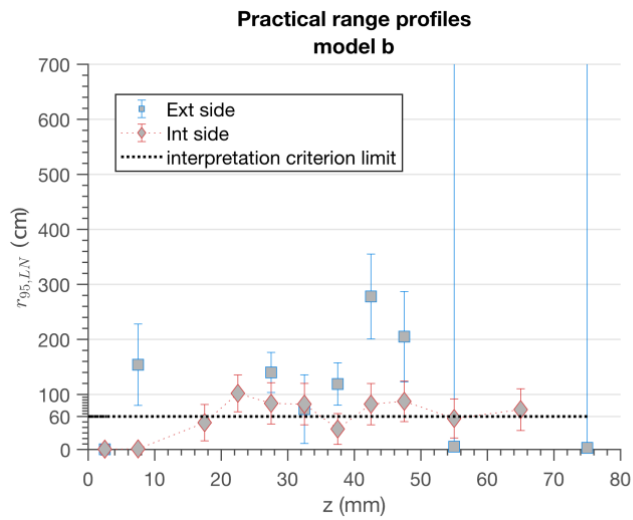
928 Figure 14 - Study of the Signal to Noise Ratio - model a

928



929 *Figure 15 - Profiles of the evolution of the mean and standard deviation of total chloride concentrations*  
 930 *according to the depth of embedding - model b*

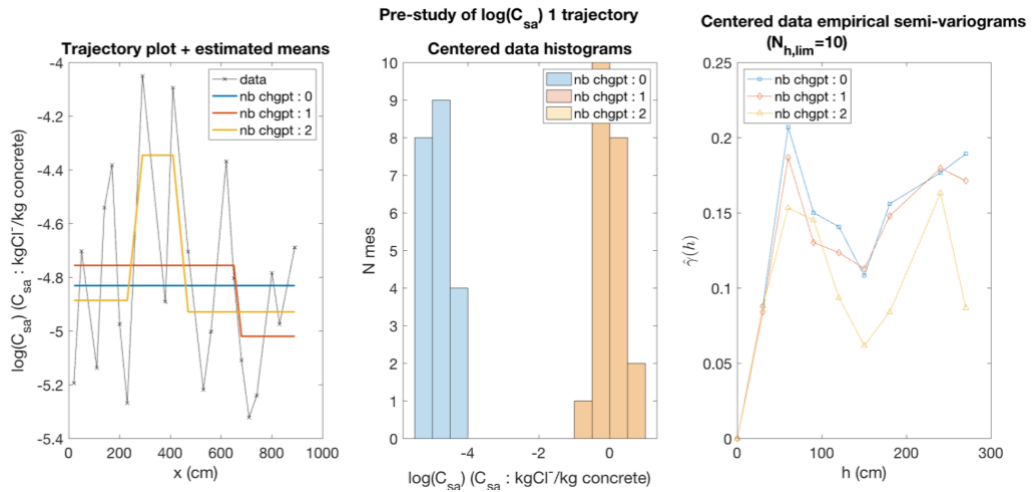
931



932  
 933 *Figure 16 - Practical range profiles of total chloride concentration trajectories as a function of embedment*  
 934 *depth - model b*

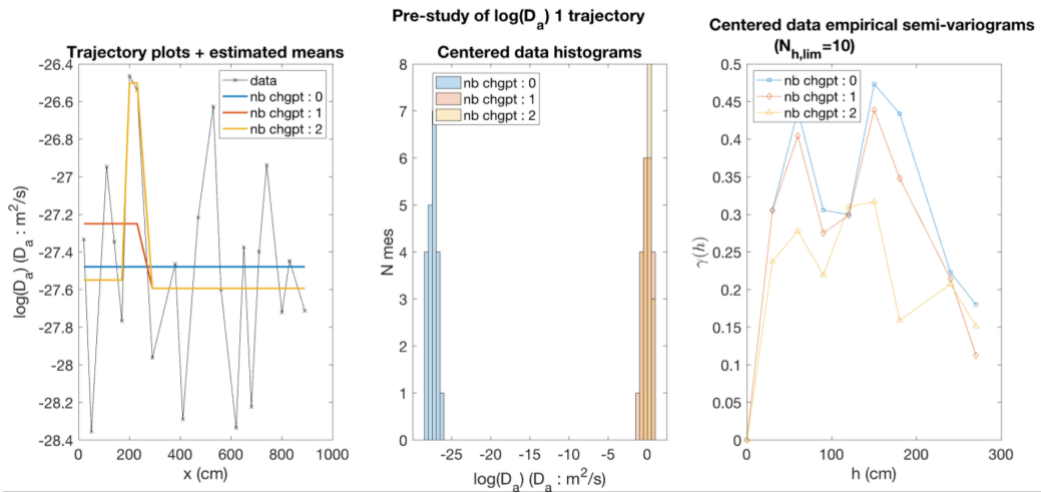
935

936



937 *Figure 17- Data and averages of trajectory 1 of log mean surface concentration; histograms of trajectories so*  
938 *centered; experimental semivariograms of trajectories so centered*

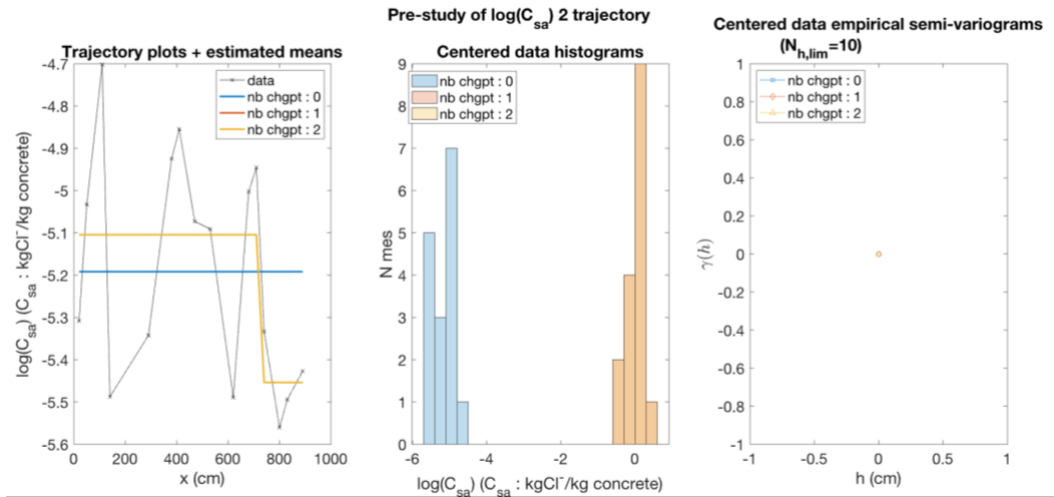
939



940 *Figure 18- Data and averages of trajectory 1 of logarithm of mean diffusivity; histograms of trajectories so*  
941 *centered; experimental semivariograms of trajectories so centered*

942

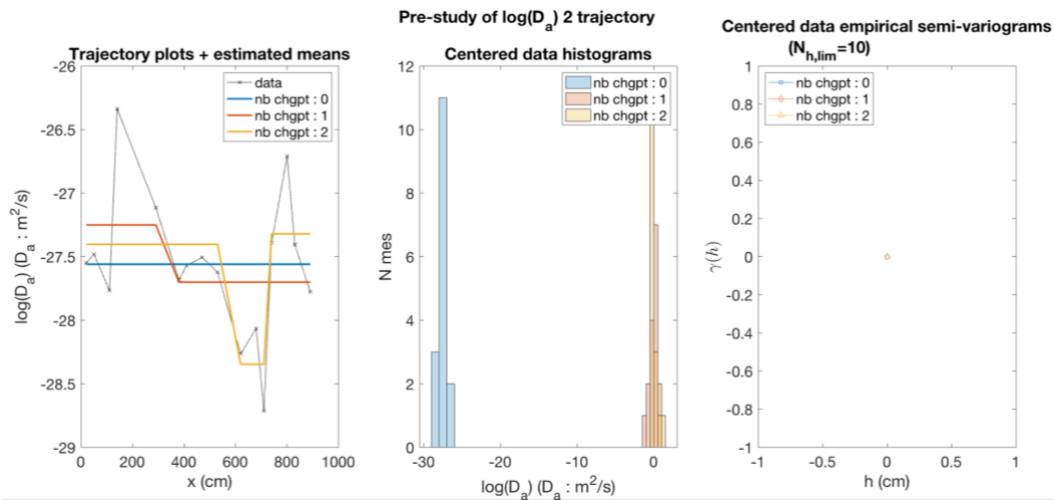
943



944  
945

Figure 19- Data and averages of logarithm of mean surface concentration trajectory 2; histograms of trajectories so centered; experimental semivariograms of trajectories so centered

946



947  
948

Figure 20- Data and averages of trajectory 2 of logarithm of mean diffusivity; histograms of trajectories so centered; experimental semivariograms of trajectories so centered

949